

## ABSTRACT

Title of Thesis:       MAGNETOSTRICTION AND MAGNETIC  
                              ANISOTROPY OF  $\text{Fe}_{35}\text{Co}_{65}$

Tong Ren, Master of Science, 2011

Thesis directed by: Professor Manfred Wuttig

Materials Science and Engineering Department

A  $\text{Fe}_{35}\text{Co}_{65}$  single crystal has been prepared by a long time anneal at temperature close to its fcc-bcc phase boundary. Its magnetostriction constant  $\lambda_{100}$  and magnetocrystalline anisotropy constant  $K_1$  was measured using a strain gauge rosette and magnetization and torque magnetometer curves. The magnetostriction constant  $\lambda_{100}$  is as high as 200 ppm. The value of the anisotropy constant  $K_1$  and the value of the susceptibility were small and influenced by the magnetoelastic energy. The symmetry of the torque curves changes from 2-fold to 4-fold with increasing external field which indicates the existence of a second uniaxial phase. This result can be interpreted by the alignment of the magnetization of an epitaxial fcc precipitate in the bcc host by external field.

MAGNETOSTRICTION AND MAGNETIC  
ANISOTROPY OF  $\text{Fe}_{35}\text{Co}_{65}$

by

Tong Ren

Thesis submitted to the Faculty of the Graduate School of the  
University of Maryland, College Park in partial fulfillment  
of the requirements for the degree of  
Master of Science  
2011

Advisory Committee:

Professor Manfred Wuttig, Chair

Professor Alison Flatau

Professor Abdellah Lisfi

Professor James R. Cullen

© Copyright by

Tong Ren

2011

**DEDICATION**  
TO MY GRANDMOTHER

## ACKNOWLEDGEMENT

First and foremost, I would like to thank my advisor Dr. Manfred Wuttig for his unwavering support and invaluable mentor through all the time of my graduate study. Without his guidance and encouragement, I can never come to this point.

I would like to thank Dr. Abdellah Lisfi for his knowledgeable advices and encouragement throughout the process of this study. I would like to thank Dr. James R. Cullen for his thoughtful suggestions during the writing. I would like thank Dr. Alison Flatau for her help and suggestions.

I would like to acknowledge the assistance of Ganesh Raghunath, Chaitanya Mudivarthi and Ernest P. Stewart Jr. for helping me through the experimental procedures required for this study. Many thanks to my fellow group members: Yueying Liu, Yemei Han, Richard Bergstrom Jr., Elizabeth Cantando for their help, support and suggestions.

Finally I must thank my parents, families and my boyfriend for their support and encouragement.

# TABLE OF CONTENTS

<b>TABLE OF CONTENTS .....</b>	<b>iii</b>
<b>LIST OF TABLES.....</b>	<b>v</b>
<b>LIST OF FIGURES.....</b>	<b>vi</b>
<b>Chapter 1 Introduction .....</b>	<b>1</b>
1.1 Iron-Cobalt (Permendur).....	1
1.2 Related Work on Iron-Gallium .....	7
1.3 Motivation.....	11
<b>Chapter 2 Sample Preparation and Measurement Technique .....</b>	<b>13</b>
2.1 Sample Preparation .....	13
2.2 Measurement Technique.....	15
2.2.1 <i>Vibrational Sample Magnetometer (VSM)</i> .....	15
2.2.2 <i>Torque Magnetometer (TMM)</i> .....	16
2.2.3 <i>Strain Gauge Measurements of Magnetostriction</i> .....	18
2.2.4 <i>Kerr-effect Optical Microscopy</i> .....	19
<b>Chapter 3 Results.....</b>	<b>23</b>

3.1 Vibrating Sample Magnetometer Data .....	23
3.2 Torque Magnetometer.....	26
3.3 Magnetostriction .....	32
<b>Chapter 4 Discussion .....</b>	<b>34</b>
<b>Chapter 5 Conclusion and future work.....</b>	<b>41</b>
<b>Appendix 1: Result Figures (sample 1-2 to 1-4).....</b>	<b>43</b>
<b>Appendix 2: Magnetic Domain Structures.....</b>	<b>55</b>
<b>References.....</b>	<b>57</b>

## **LIST OF TABLES**

Table 1.1 Magnetic properties of FeCo (50:50) alloy <sup>[7]</sup>

Table 1.2 Value of anisotropy constant by Rafique et al. <sup>[36]</sup>

Table 2.1 Composition, heat treatment and dimensions of single crystal samples

Table 3.1 Rotational hysteresis presented by the difference of area of sample 1-1 to 1-4

Table 3.2 Anisotropy field and saturation field of magnetostriction for sample 1-1 to 1-4

Table 3.3 Anisotropy field and constants of single crystal Fe<sub>35</sub>Co<sub>65</sub> samples

Table 3.4 Magnetostriction at H=4000G

## LIST OF FIGURES

Figure 1-1 Magnetization curves with different crystalline orientation of iron-cobalt single crystal at different cobalt concentration <sup>[3]</sup>

Figure 1-2 Phase diagram of Fe-Co system <sup>[9]</sup>

Figure 1-3 Magnetic anisotropy constant  $K_1$  of the Fe-Co system. <sup>[7]</sup>

Figure 1-4 Magnetostriction constant as a function of at.% Co ( <sup>[22][23][24][25]</sup>)

Figure 1-5 Saturation magnetostriction as a function of annealing temperature <sup>[27]</sup>

Figure 1-6 Phase diagram of FeGa <sup>[30]</sup>

Figure 1-7 Magnetostrictive constants, (a)  $\lambda_{100}$  and (b)  $\lambda_{111}$ , for  $\text{Fe}_{1-x}\text{Ga}_x$  single crystal alloys as a function of at.% Ga <sup>[35]</sup>.

Figure 1-8 Magnetocrystalline anisotropy constant  $K_1$  as a function of concentration of Ga <sup>[36]</sup>

Figure 1-9 Magnetic domain structure revealed by Kerr Optical Microscopy <sup>[30]</sup>

Figure 1-10 The comparison of the magnetization curves at different crystalline directions of pure iron,  $\text{FeGa}_{14}$  and  $\text{FeGa}_{20}$  (a) <sup>[38]</sup>,  $\text{FeCo}_{65}$  and pure iron (b) <sup>[39]</sup>

Figure 2-1 The sample directions of the [001] disc.

Figure 2-2 Partial phase diagram of Iron-Cobalt alloys <sup>[9]</sup>

Figure 2-3 The vibrating sample magnetometer block diagram

Figure 2-4 The scheme of torque measurements

Figure 2-5 The block diagram of torque magnetometer

Figure 2-6 The scheme of longitudinal Kerr-effect<sup>[41]</sup>

Figure 2-7 The scheme of transverse Kerr-effect<sup>[41]</sup>

Figure 2-9 The wide field microscopy set ups<sup>[30]</sup>

Figure 3-1 The magnetization curves of [n-001] single crystal sample 1-1

Figure 3-2 The coercivity of sample 1-1

Figure 3-3 Torque curves of sample 1-1 at 600G

Figure 3-4 Torque curves of sample 1-1 at 800G

Figure 3-5 Torque curves of sample 1-1 at 1000G

Figure 3-6 Torque curves of sample 1-1 at 1500G

Figure 3-7 Polar plot of sample 1-1, at different magnetic field (a) 600G, (b)800G, (c)1000G and (d)1500G

Figure 3-8 Magnetostriction of sample 1-1 under H field applied along  $\hat{x}$  (left) and  $\hat{y}$  (right)

Figure 3-9 Magnetostriction of <110> direction of sample 1-3 under H field applied along <110> direction

Figure 4-1 Comparison between the amplitude of T2 and T4 vs field and the magnetostriction vs field

Figure 4-2 Normalized torque curves  $T(\theta)$  of sample 1-2 obtained at four increasing magnetic fields

Figure 4-3 Symmetry of the presented crystal

# Chapter 1 Introduction

## 1.1 Iron-Cobalt (Permendur)

Iron-cobalt alloys are known to have the highest saturation magnetization among all magnetic materials <sup>[1]</sup>, high permeability <sup>[2]</sup>, and low hysteresis <sup>[3]</sup>. The high saturation magnetization enables them to induce large attractive forces to operate moving parts and be candidates for electro-mechanical applications as well <sup>[4]</sup>. The coercivity of iron-cobalt is influenced strongly by its microstructures <sup>[5][6]</sup>, like in all other soft materials.

Equiatomic iron-cobalt alloys were named “Permendur” by Elmen <sup>[2]</sup>, 1927. The permendur alloy was found to have a slightly lower saturation magnetization, a much higher permeability and a lower coercivity than the Fe<sub>2</sub>Co alloy <sup>[7]</sup>. The maximum saturation magnetization of iron-cobalt alloy system reaches almost 2.4T at around 35at.% of cobalt <sup>[4]</sup>. The initial permeability reaches its maximum at 50at.% of cobalt (Permendur) <sup>[8]</sup> and stays constant regardless of heat treatment temperature, while the maximum permeability was found to be highest in permendur after it has been annealed at 850° C and furnace cooled <sup>[1]</sup>.

The anisotropy of the magnetization curves has been studied using a pendulum magnetometer by J.W.Shih et al. <sup>[3]</sup> on iron-cobalt single crystal alloys and the results are shown in figure 1-1. The alloys show an easiest direction of magnetization along <100> axes, as is typical for bcc crystals, at 30 at.% and 40 at.% of cobalt and they show an easy direction of magnetization of <111> axes at 50at.% and 70at.% of cobalt. The maximum hysteresis was reported to be as low as  $7 \times 10^3 \text{ ergs} \cdot \text{cm}^{-3}$  <sup>[3]</sup>.

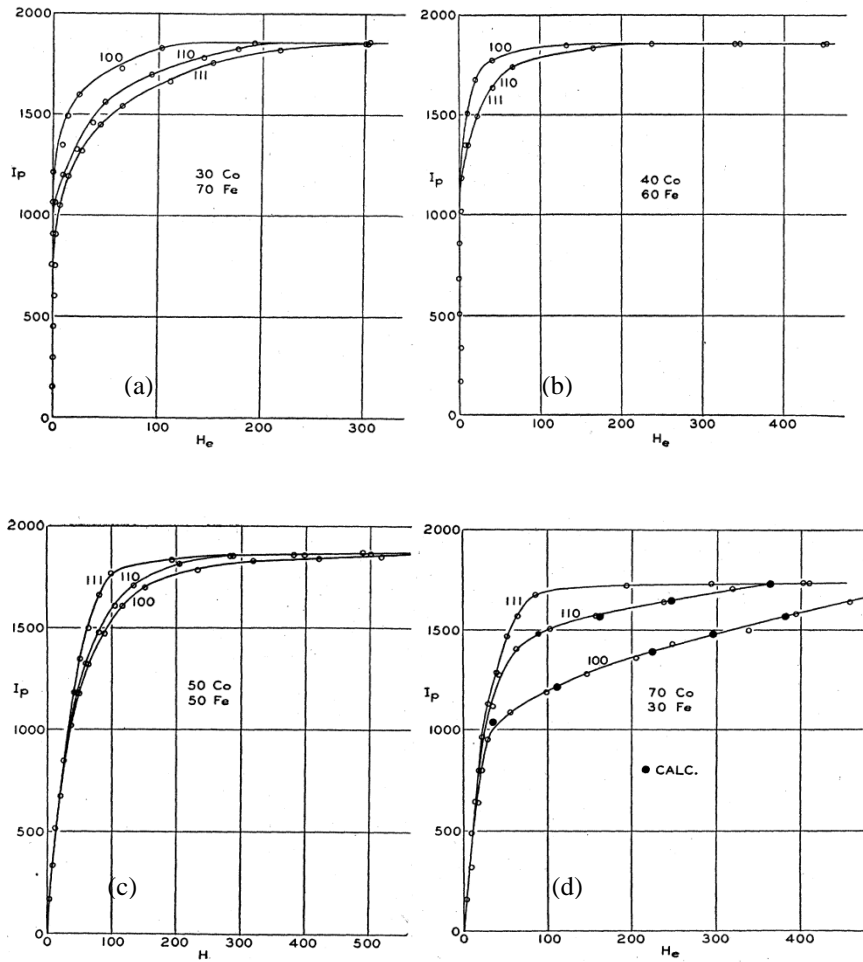


Figure 1-1 Magnetization curves with different crystalline orientation of iron-cobalt single crystal at different cobalt concentration, i.e., (a)30at.% , (b)40at.% , (c)50at.% , (d) 70at.% , respectively. <sup>[3]</sup>

In order to obtain a better understanding towards the complex relationship between different phases' structures and particularly the magnetostriction exhibited by them, the basic metallurgical aspects of the iron-cobalt system are important to know.

Figure 1-2 shows the equilibrium phase diagram of Fe-Co system <sup>[9]</sup>. At room temperature <sup>[3]</sup>, the hcp structure forms in alloys containing less than 5 at.% Fe; the fcc structure forms at 5-22 at.% Fe; and the bcc structure at 22-100 at.% Fe. At 500°C, a two phase (fcc+bcc) region,  $\alpha + \gamma$ , containing of Co rich  $\gamma$  and Fe rich  $\alpha$  forms. The bcc-  $\alpha$  (A2)

mono-phase forms beyond 23at.% of Fe except for the region of 28-75at.% Fe, where ordered bcc-  $\alpha'$  (B2) phase forms. At higher temperature above 985°C,  $\delta$  (bcc) and  $\gamma$  (A1) phases exists. At temperature lower than 500°C,  $\epsilon$  phase exists within 0-6 at% Fe and the  $\gamma + \epsilon$  and  $\alpha + \epsilon$  two phases regions exist with 6-8 at% Fe and 8-23at% Fe respectively. The lattice parameter decreases with increasing Co concentration.

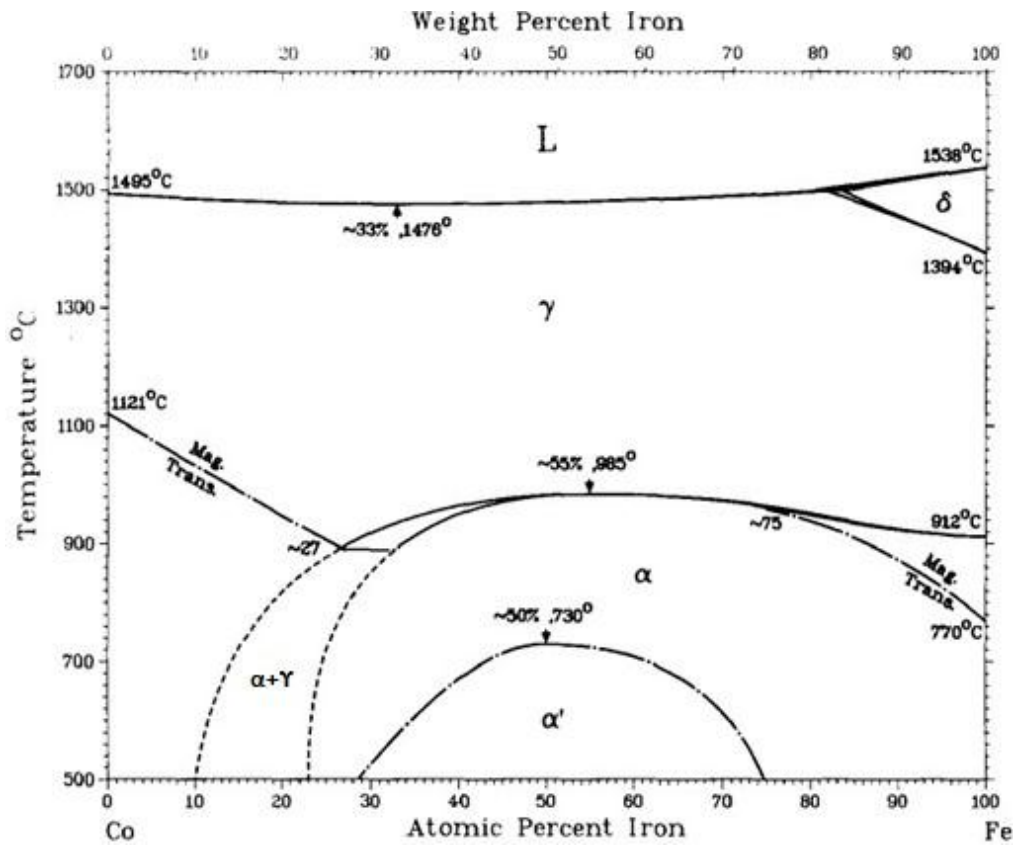


Figure 1-2 Phase diagram of Fe-Co system<sup>[9]</sup>

The Curie temperature of  $\text{Fe}_{1-x}\text{Co}_x$  alloys coincides with the  $\alpha$  to  $\gamma$  phase transition temperature<sup>[4]</sup> and depends on the cobalt concentration. The maximum Curie temperature is 985°C at 46 at.% of Co<sup>[4]</sup>.

Evidence for ordering was presented by several researchers since 1939<sup>[10][11][12]</sup>. The maximum order-disorder transformation temperature was reported as 732 °C by Ellis and Greiner<sup>[13]</sup>. The ordering reaction in equiatomic FeCo is very rapid above 500°C<sup>[8]</sup>, but could be totally avoided by quenching above 800 °C with quenching rates greater than ~4000 °C/s<sup>[14]</sup> (700µm as thickness). The lattice parameter expands with the decreasing of Co concentration because of ordering in the B2 phase.<sup>[15][16]</sup>

Fe-Co alloys have low magnetocrystalline anisotropy<sup>[17]</sup>. Figure 1-3 shows the magnetic anisotropy of BCC Fe-Co alloys<sup>[18][19]</sup> measured by a torque magnetometer. It can be seen that the magnetic anisotropy constant  $K_1$  decreases as the Co concentration increases and changes its sign at ~42at% of cobalt for the disordered phase. Furthermore, the value of  $K_1$  approaches zero for ordered Fe-Co (50:50) alloys<sup>[19]</sup>. The magnetic anisotropy of permendur is relatively low,  $K_1 = -1 \times 10^5 \text{ J/M}^3$  (disordered) and  $K_1 = 0$  (ordered)<sup>[20]</sup>. Additional uniaxial anisotropy energy has been observed by Chamberod et al.<sup>[21]</sup> in 1972, when the heat treatment was carried out under an applied magnetic field.

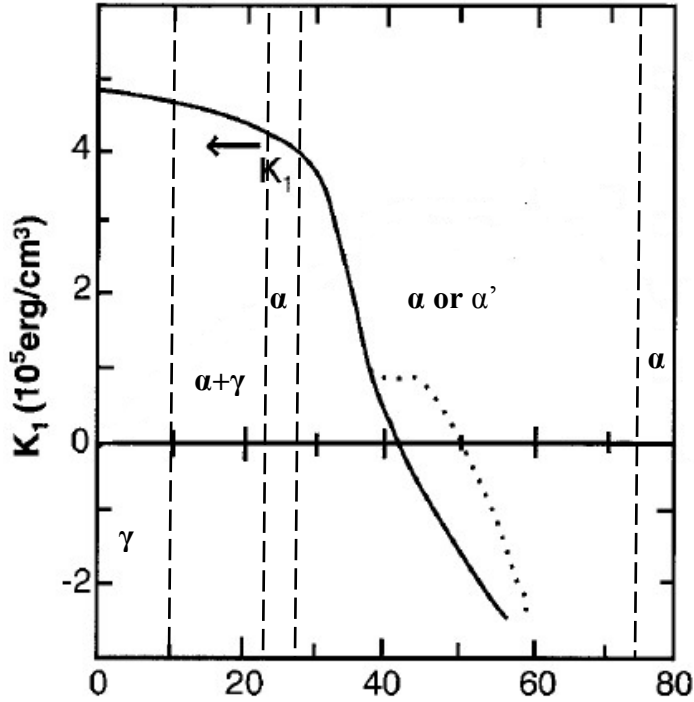


Figure 1-3 Magnetic anisotropy constant  $K_1$  of the Fe-Co system; dot line is the anisotropy constant for the ordered B2 phase. Dash lines show the regions of different phases at 500 C. (reprinted from ref. 7)

The magnetostriction of slow cooled polycrystalline Co-Fe alloys was reported by Williams<sup>[22]</sup> and Masiyama<sup>[23]</sup> in 1932. According to these reports a maximum strain of 60 to  $90 \times 10^{-6}$  was found. The highest value at that time was observed by Nesbitt<sup>[24]</sup> in order of  $130 \times 10^{-6}$  on hard rolled  $\text{Fe}_{30}\text{Co}_{70}$  alloys. A more detailed research of the magnetostriction constant of FeCo single crystals was conducted by Helen M. A. Urquhart et al. in 1953<sup>[25]</sup>. Alloys in the concentration range of 0 to 70 at.% cobalt were measured and calculated using the Bates and Lee's method<sup>[26]</sup> from polycrystalline samples for the composition range, in which single crystals were not available. However, the heat treatment procedure of these samples was not mentioned. The magnetostriction constant of  $\text{Fe}_{1-x}\text{Co}_x$  as a function of Co concentration obtained from polycrystalline samples and single crystal samples are reproduced in figure 1-4.

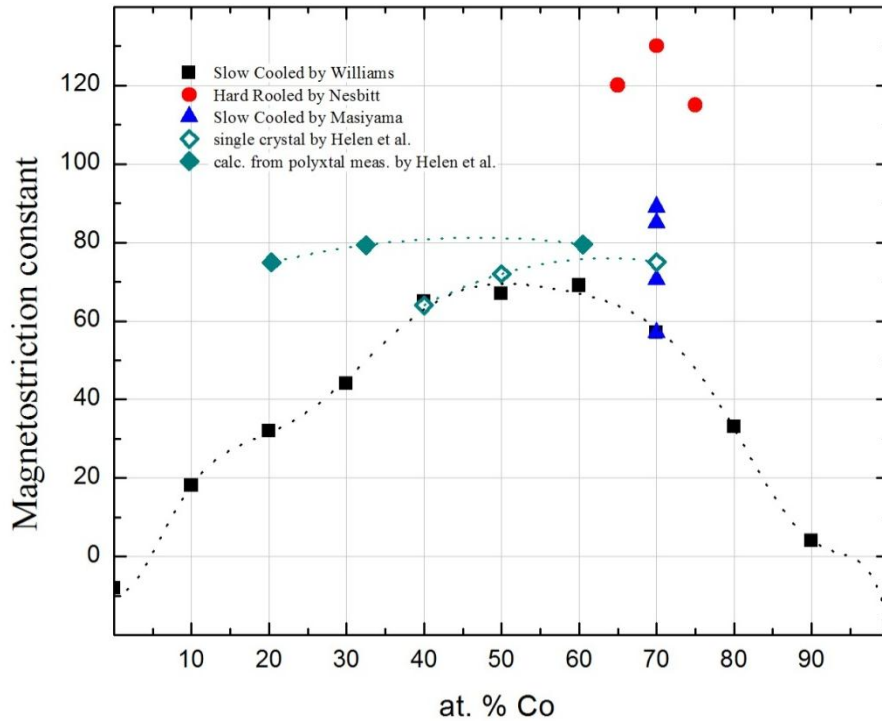


Figure 1-4 Magnetostriction constant as a function of at.% Co (reprinted from ref. [22][23][24][25])

More recently, higher saturation magnetostriction up to  $147 \times 10^{-6}$  for  $\text{Fe}_{1-x}\text{Co}_x$  alloys on the cobalt rich side ( $\text{Fe}_{30}\text{Co}_{70}$ ) were reported by Dai and Wuttig, 2007<sup>[27]</sup>. According to this article, the highest value of  $\lambda_{100}$ , observed when quenching from temperature near the bcc// bcc/(hcp+bcc) phase boundary, is believed to be similar in origin to the large saturation magnetostriction observed from FeGa alloys<sup>[28]</sup>. Figure 1-5 is the saturation magnetostriction as a function of the annealing temperature according to Dai and Wuttig.

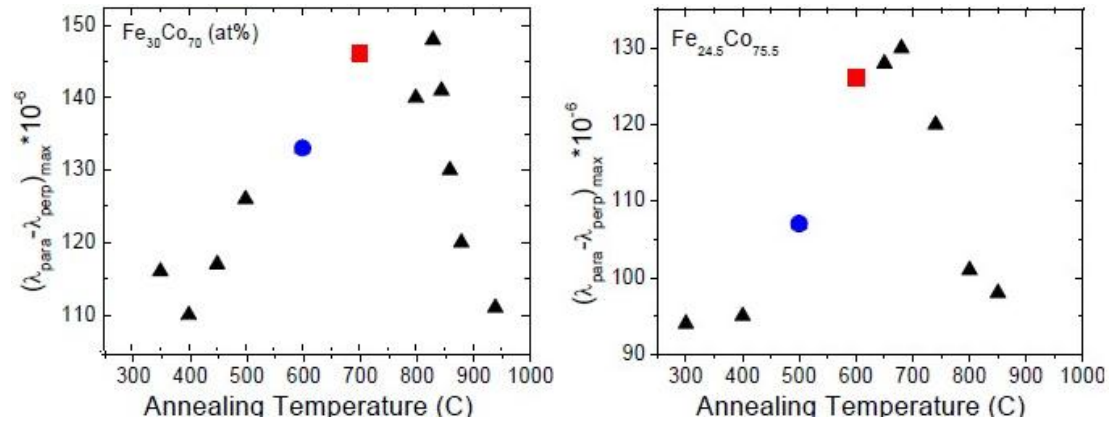


Figure 1-5 Saturation magnetostriction as a function of annealing temperature <sup>[27]</sup>

A summary of permendur is given in Table 1.1 <sup>[7]</sup>, showing some important magnetic properties of FeCo (50:50) alloy.

Property	Value
Curie temperature (°C)	980
Saturation magnetisation (T)	2.4
Coercivity (A m <sup>-1</sup> )	150
Initial permeability	800
Maximum permeability	5000–8000
Saturation magnetostriction (ordered condition) $\lambda_{100}$	$150 \times 10^{-6}$
$\lambda_{111}$	$25 \times 10^{-6}$
$\lambda_{polycrystal}$	$60 \times 10^{-6}$
Magnetocrystalline anisotropy constant (J m <sup>-3</sup> )	0

Table 1.1 Magnetic properties of FeCo (50:50) alloy <sup>[7]</sup>

## 1.2 Related Work on Iron-Gallium

For a more detailed summary of the past research work done on iron-gallium, Datta's dissertation <sup>[29]</sup> or Mudivarthi's dissertation <sup>[30]</sup> can be consulted. Only the research work related to this thesis will be discussed here.

Figure 1-6 is the phase diagram of  $\text{Fe}_x\text{Ga}_{1-x}$ . From the phase diagram, we can see that at room temperature, the alloy forms disordered bcc (A2) phase between 0at.% and 12 at. % Ga. A mixture of the  $\text{Fe}_3\text{Ga}$  (L12) phase and the A2 phase exists between 12at.% and 25 at% of Ga. Only at high temperature (above  $588^\circ\text{C}$ ), phases as  $\text{D0}_3$ , B2, B2' and  $\text{Fe}_3\text{Ga}$  ( $\text{D0}_{19}$ ) exist.

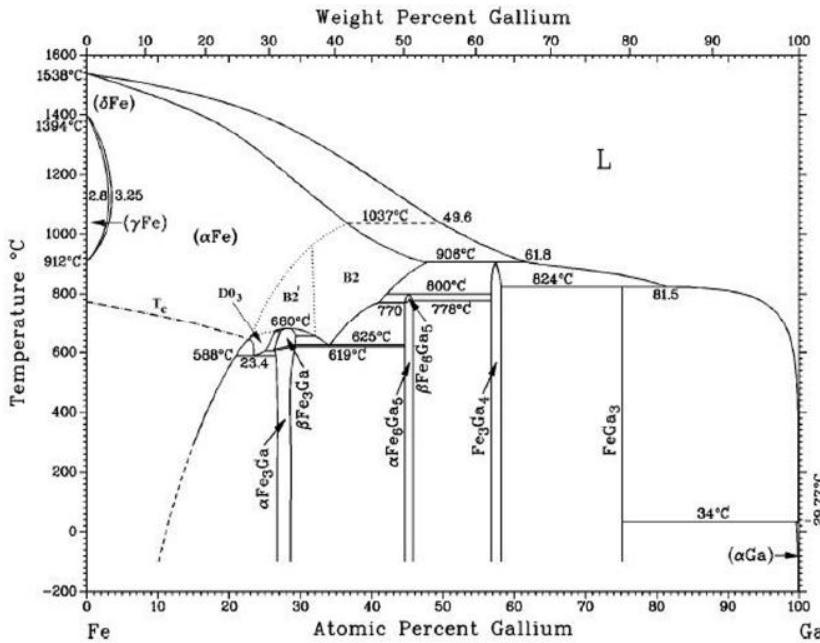


Figure 1-6 Phase diagram of  $\text{FeGa}$  [30]

The non-magnetic addition of Gallium into the pure iron increases the value of magnetostriction of iron more than tenfold similar to the addition of aluminum [32]. In addition to their large magnetostriction, the  $\text{Fe}_{1-x}\text{Ga}_x$  alloys exhibit ductile-like behavior [31], high tensile strengths ( $\sim 400$  MPa) [32,33], low saturation fields ( $\sim 10$  mT) [31,34] and low hysteresis [31][30]. Figure 1-8 shows the change of magnetostriction constant as a function of the atomic percentage of gallium. The influence of different ways of heat

treatments is shown in figure 1-7 as well. The two peaks of magnetostriction occur at 20at.% Ga and 28at.% Ga respectively for the quenched alloys.

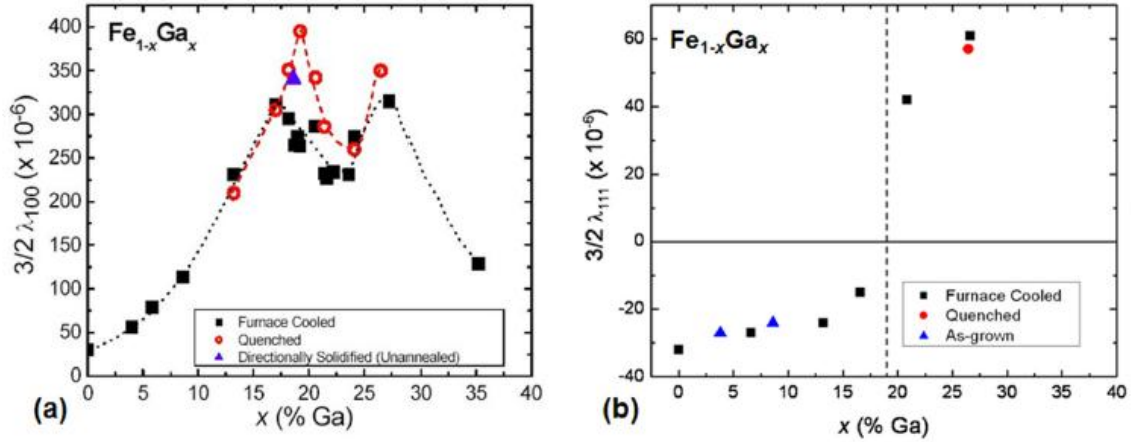


Figure 1-7 Magnetostrictive constants, (a)  $\lambda_{100}$  and (b)  $\lambda_{111}$ , for Fe<sub>1-x</sub>Ga<sub>x</sub> single crystal alloys as a function of at.% Ga<sup>[35]</sup>.  $\lambda_{100}$  exhibits two peaks, where the first one is highly dependent to the thermal history.

The magnetocrystalline anisotropy changing with Ga concentration was measured by Rafique et al.<sup>[36]</sup>. As shown in figure 1-8, the anisotropy constant  $K_1$  decreases to almost zero at 20at.% of Ga, where the magnetostriction reached the first maximum. Table 1.2 shows the experimentally determined value of  $K_1$  at different Ga concentration.

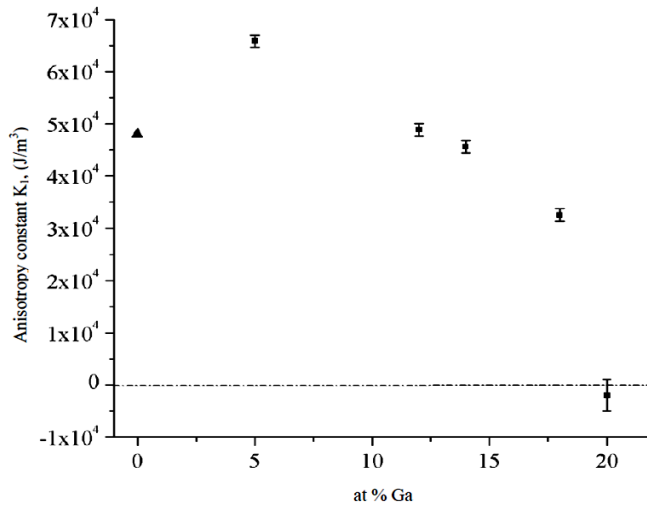


Figure 1-8 Magnetocrystalline anisotropy constant  $K_1$  as a function of concentration of Ga<sup>[36]</sup>

Composition	Saturation Magnetization	$K_1$ From {110} Disk	$K_1$ From {100} Disk
at.% Ga in Fe	emu/cc	J/m <sup>3</sup>	J/m <sup>3</sup>
0	1745*	$4.8 \times 10^4$	
5	1745	$6.56 \times 10^4$	$6.26 \times 10^4$
12.5	1590	$4.88 \times 10^4$	$4.63 \times 10^4$
14	1575	$4.56 \times 10^4$	$4.38 \times 10^4$
18	1406	NA	$3.49 \times 10^4$
20	1343	$-2 \times 10^3$	$3.23 \times 10^2$

Table 1.2 Value of anisotropy constant by Rafique et al.<sup>[36]</sup>

Recently, the 'real' domain structures of  $Fe_xGa_{1-x}$  alloys, shown in figure 1-9, were revealed using Kerr Optical Microscopy by Mudivartha et al.<sup>[30]</sup> after careful mechanical polishing. The domains oriented along [100],  $[\bar{1}00]$ , [010] and  $[0\bar{1}0]$  show 90° and 180° domain walls. From these results, the magnetic domain structures exhibit no unusual behavior and their evolution are closely tracked the samples' magnetostriction properties.

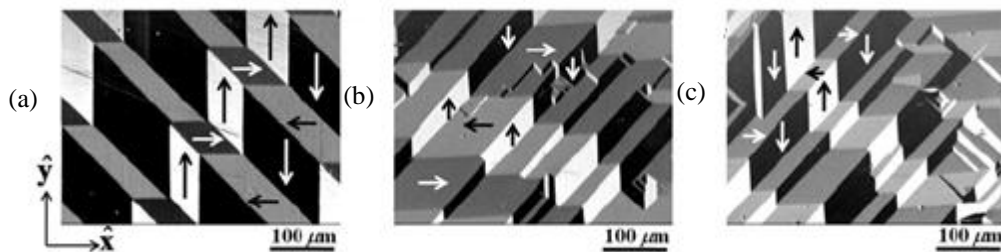


Figure 1-9 Magnetic domain structure revealed by Kerr Optical Microscopy (reprinted from ref. [30]). (a) and (b) both have 17at.% of Ga while (c) has 19at.% of Ga. (a), (b) and (c) were all annealed at 1000°C for 4 hrs and quenched except that (a) was cooled at 10°C/s.

### 1.3 Motivation

The technically interesting high values of the magnetostriction and the good elastic properties of iron-gallium alloy system make FeGa attractive materials for sensor applications. Magnetostriction of FeGa alloys has been found to be as high as  $400\mu\epsilon$ <sup>[37]</sup>, twice as much of that for FeAl alloys<sup>[32]</sup>. FeGa alloys were reported to be magnetically soft, the value of the magnetocrystalline anisotropy constant  $K_1$  decrease dramatically beyond certain level of substituting Fe by Ga. It has also been found that the magnetization curves of iron-gallium<sup>[38]</sup> alloys at certain compositions are very different from the well-known magnetization curves of soft magnetic materials such as iron<sup>[39]</sup>. The FeGa<sub>20</sub><sup>[38]</sup> alloy shows  $\langle 110 \rangle$  easy axes of magnetisation on the (001) plane instead of the  $\langle 100 \rangle$  easy axes of pure iron. Moreover, the experimentally determined magnetocrystalline anisotropy constant  $K_1$  of FeGa<sub>20</sub> alloy<sup>[36]</sup> is almost zero. As is shown in Figure 1-10(a), the slopes of the magnetization curves for FeGa alloys are relatively small when comparing them with pure iron.

Our original motivation is to find a higher magnetostriction on the Fe<sub>35</sub>Co<sub>65</sub> single crystal by annealing at temperature close to the  $\alpha+\gamma/\alpha$  phase boundary and quench it to obtain the twin structures. During experiments, a similar trend of the magnetization curves similar to FeGa has been found in the high magnetostrictive iron-cobalt system as is shown in Figure 1-10(b). It appeared desirable to investigate FeCo single crystal alloys in both magnetic and structural aspects to gain a better understanding of the physical origin of this phenomenon.

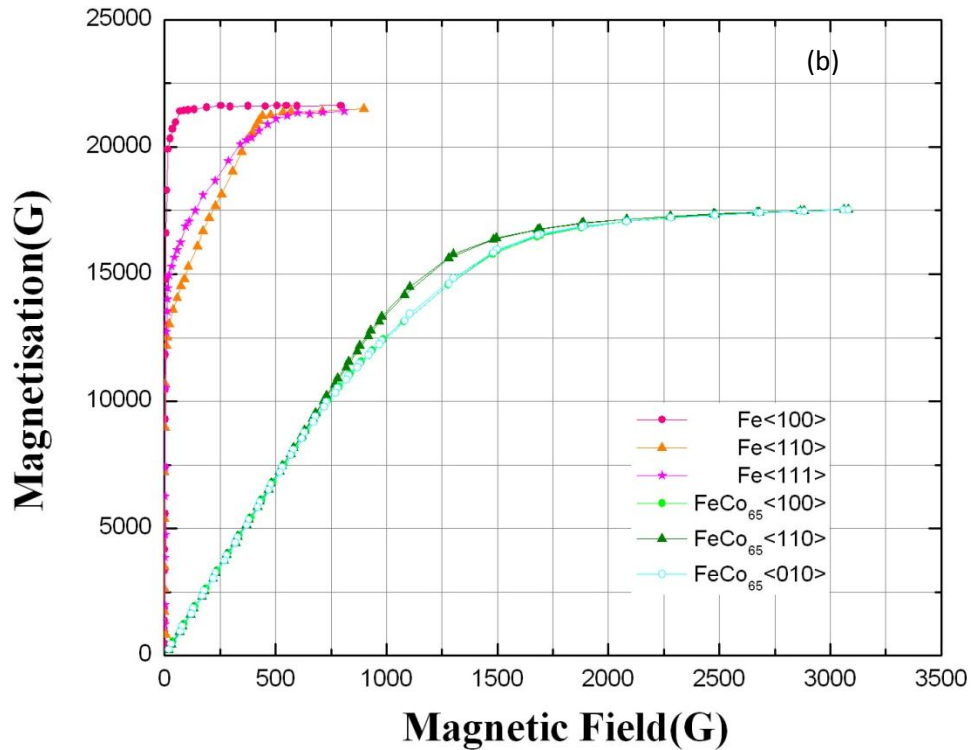
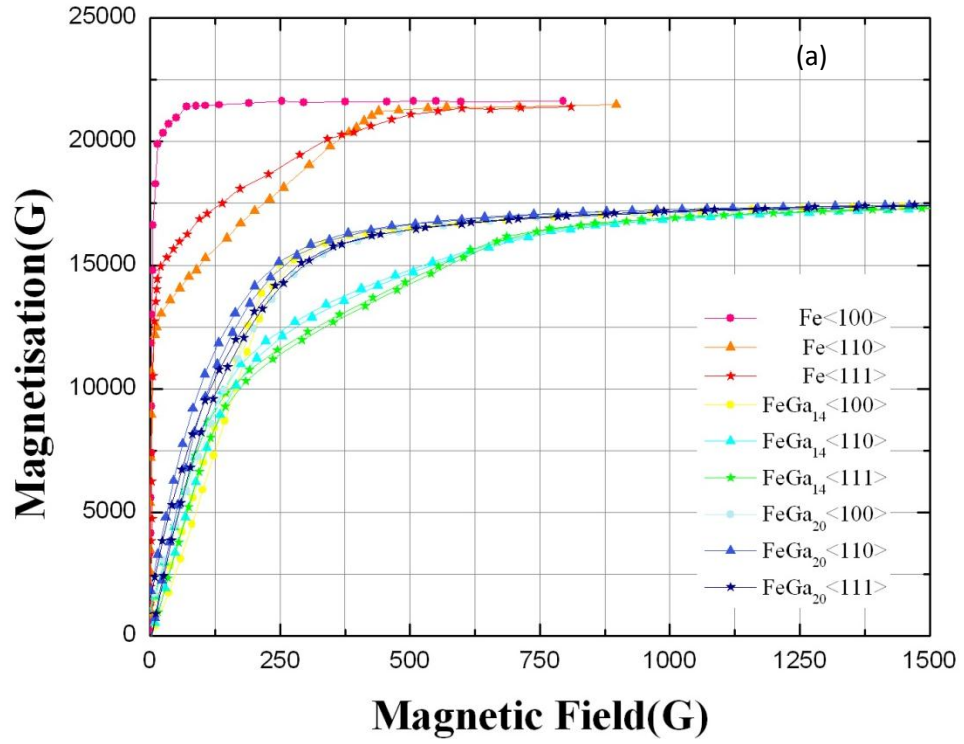


Figure 1.10 The comparison of the magnetization curves at different crystalline directions of pure iron, FeGa<sub>14</sub> and FeGa<sub>20</sub> (a) <sup>[reprinted from ref. 38]</sup>, FeCo<sub>65</sub> and pure iron (b) <sup>[reprinted from ref. 39]</sup>

## Chapter 2 Sample Preparation and Measurement Technique

### 2.1 Sample Preparation

The  $\text{Fe}_{35}\text{Co}_{65}$  single crystal specimen was prepared by T.A. Lograsso and D.L. Schlager in Materials & Engineering Physics Program of the Ames Laboratory, using the Bridgmann technique. Grain growth was achieved by annealing the sample at  $1050^\circ\text{C}$  for 0.5 hr, followed by a one week annealing at  $860^\circ\text{C}$ . The sample was then slow cooled at a rate of  $10^\circ\text{C}/\text{min}$ . The orientation of the cylinder specimen was determined by back reflection Laue measurements and is shown in Figure 2-1. One set of four circular disks with  $\langle 100 \rangle$  normal were cut from this original sample by Electrical Discharging Machining (EDM).

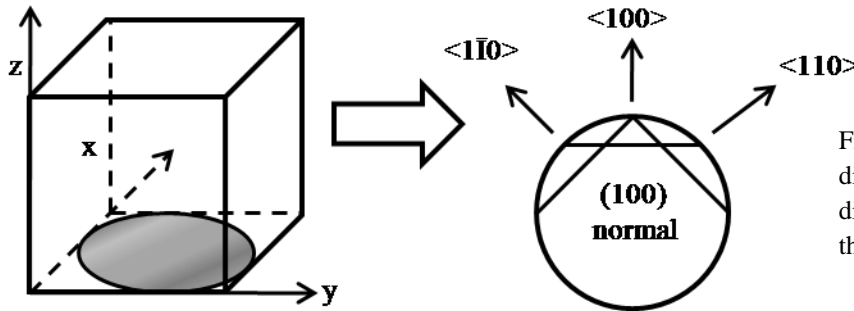


Figure 2-1 The sample directions of the [001] disc. (Only be kept on the sample 1-1)

The four  $\text{Co}_{65}\text{Fe}_{35}$  single crystal disks were annealed at different temperatures with different annealing times in a 'Carbolite' furnace under argon flowing (as protection) and then quenched in to cold water ( $<10^\circ\text{C}$ ). Figure 2-2 is the phase diagram of iron-cobalt, in which the annealing temperatures of sample disks 1-2, 1-3 and 1-4 are marked. As reported by Dai and Wuttig (2007)<sup>[27]</sup>, the magnitude of the magnetostriction depends on the state of the alloy and reaches a maximum for  $\text{Fe}_{30}\text{Co}_{70}$  polycrystalline samples, when annealed close to the bcc/ (fcc+bcc) phase boundary. The annealing temperatures of

875°C and 790°C, which are close to the bcc/(fcc+bcc) phase boundary, were chosen for single crystal sample disks 1-2 and 1-3, respectively. 300°C for sample disk 1-1 and an intermediate temperature of 690°C for sample disk 1-4, were chosen as reference. Table 2.1 gives the annealing conditions and also dimensions of the four single crystal sample disks.

Sample	Annealing Temperature (°C)	Annealing Time (minutes)	Diameter (mm)	Thickness (mm)	Thickness(mm) (*)
1-1	300	3800	5.93	0.53	0.445
1-2	875	20	5.95	0.51	0.439
1-3	790	50	5.94	0.53	0.300
1-4	690	60	5.95	0.50	0.371

Table 2.1 Composition, heat treatment and dimensions of single crystal samples

\* Thickness of samples after polishing for Kerr Microscopy measurements. Data of magnetization and magnetostriction measurements were obtained after polishing.

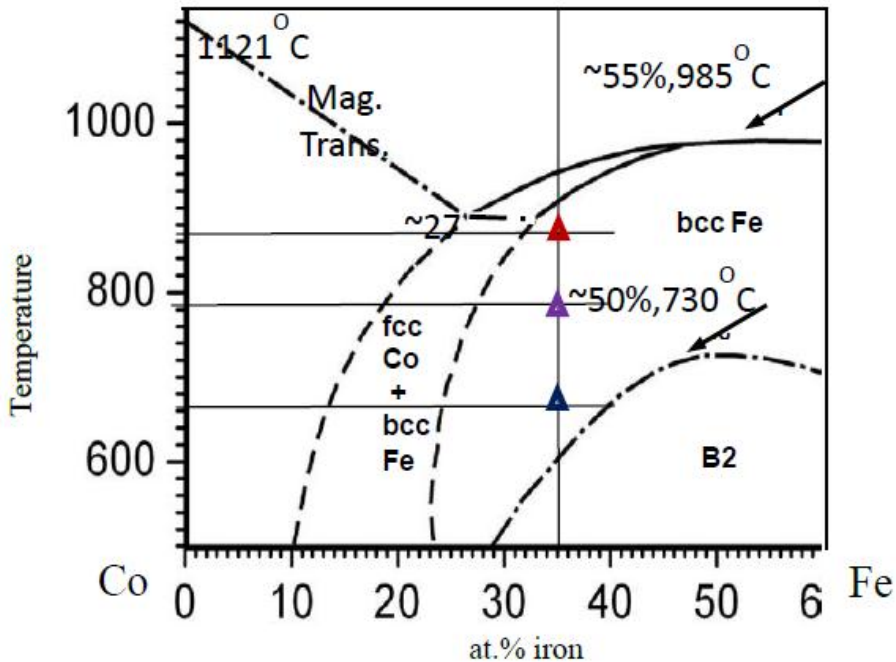


Figure 2-2 Partial phase diagram<sup>[9]</sup> of Iron-Cobalt alloys. ▲ refers to sample 1-2; ▲ refers to sample 1-3; and ▲ refers as sample 1-4.

## 2.2 Measurement Technique

### 2.2.1 Vibrational Sample Magnetometer (VSM)

A VSM is designed to measure the magnetization. The sample is magnetized inside a uniform magnetic field and then physically vibrated as a function of time. The vibration will cause a change in the magnetic field caused by the sample, which causes an induced voltage in the pick-up coils. Thus, the induced voltage of the pick-up coils will be proportional to the sample's magnetic moment. The signals is amplified by a differential amplifier and a lock-in amplifier and then be transferred to the computer. The whole system is controlled by a Lab-VIEW program. One can set up the steps of the time-related magnetization progress and also the angle between the direction of the sample and the external magnetic field by simply changing the parameters in the operation recipe.

Figure 2-3 shows the block diagram of the VSM.

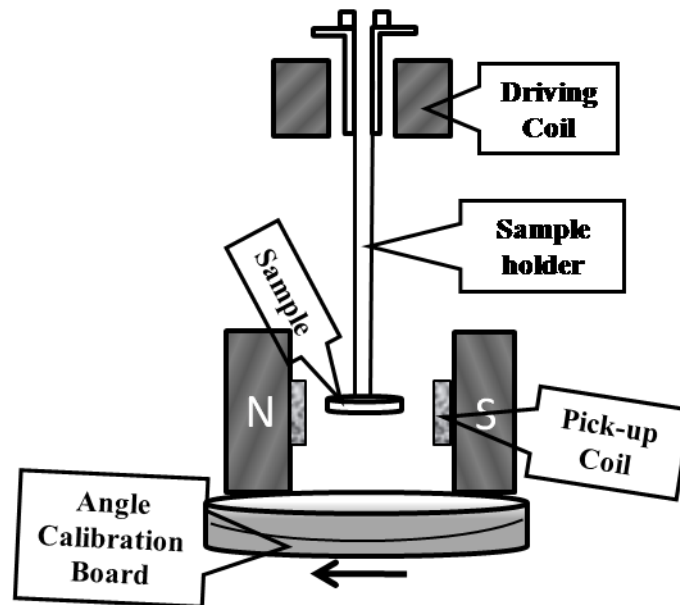


Figure 2-3 The vibrating sample magnetometer block diagram

### 2.2.2 Torque Magnetometer (TMM)

A torque magnetometer was used to make torque measurements to determine the anisotropy more accurately than the conventional magnetometer. The principle of this measurement is based on a torque balance. On one hand, when the magnetic field applied, the magnetic moments inside of the sample will tend to align themselves along the same direction as the external field. The anisotropy of the sample, on the other hand, will try to pull the magnetization along the direction of the easy axis of the sample, which causes a torque (force) on the sample. When the directions of external field and easy axis coincide, the value of the torque is zero. But when the two directions do not coincide, the torque is not zero and its value can be measured by the torque magnetometer. The scheme of torque measurement is shown in figure 2-4.

Figure 2-5 is the block diagram of the torque magnetometer<sup>[40]</sup>. A sample holder with sample is hanging on a thin wire in a magnetic field, which causes the sample experiences a torque. At the top end of the sample holder, a coil is mounted between a permanent magnet of a known strength. The torque on the sample can now be compensated by a torque on the coil when a current flows through this compensation coil. Using a small mirror, a lamp and two photo diodes to detect the rotation of the sample, the current through the compensation coil is controlled. The current through the compensation coil is proportional to the torque exerted on the sample. The ADE-TMM<sup>[40]</sup> that was utilized in this study is using a virtually frictionless air bearing instead of the torsion wire as in Figure 2-5. The shape of the sample should be a cylindrical disk or a round ball, so that the sample's shape anisotropy does not influence the measurements.

The sample was mounted by double sided tape at the end of a rod shaped sample holder with a round disk shaped end and be placed between the N-S poles of the electro-magnets. The rotation angle of the magnetic field is externally controlled. The whole system is controlled by a Lab-VIEW computer program.

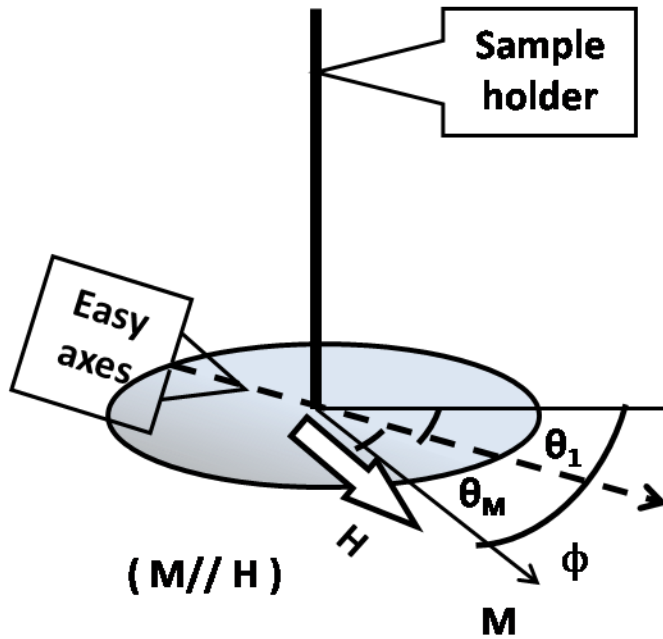


Figure 2-4 Scheme of torque measurements

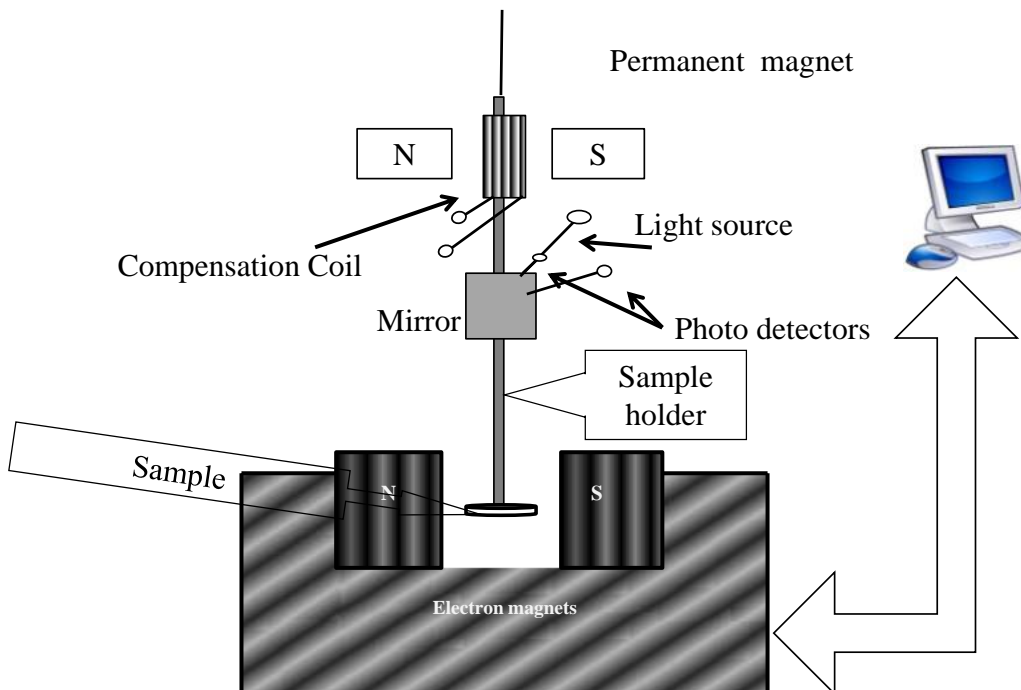


Figure 2-5 The block diagram of torque magnetometer <sup>[40]</sup>

The dependence of torque versus  $\theta_M$  (see Figure 2-4) will give a torque curve  $T = -\frac{\partial E_a}{\partial \theta_M}$

(2-1), where  $\theta$  is the angle between the direction of applied field and a reference direction (i.e. a crystallographic axis).

As we know, for the cubic crystal,

$$E_a = K_1(\alpha_1^2\alpha_2^2 + \alpha_2^2\alpha_3^2 + \alpha_3^2\alpha_1^2) + K_2\alpha_1^2\alpha_2^2\alpha_3^2,$$

where  $\alpha_1 = \sin \theta \cos \varphi$ ;  $\alpha_2 = \sin \theta \sin \varphi$ ;  $\alpha_3 = \cos \theta$ . For a (001) disk,  $\theta = \frac{\pi}{2}$ , so that, if

$\alpha_1 = \cos \varphi$ ;  $\alpha_2 = \sin \varphi$ ;  $\alpha_3 = 0$ .  $\varphi = \theta_M$ , if the easy axis is the reference direction.

therefore,

$$E_a = \frac{1}{4} K_1 \sin^2(2\theta_M) \quad (2-2)$$

and, combined with eq. (2-1),

$$T = -\frac{1}{2} K_1 \sin(4\theta_M) \quad (2-3)$$

### 2.2.3 Strain Gauge Measurements of Magnetostriction

The axes [100], [010], and [001] of the sample were aligned with respect to the x-, y-, and z- axes of a coordinate system respectively. A bidirectional resistive strain gage rosette was applied onto the surface of the sample disks to measure strain along x- and y- directions. An electromagnet was used to apply magnetic field up to 4000 G. The field was ramped up from  $\sim 0$  G (remanent field) to 4000G, then down to  $\sim 0$  G at a rate of  $\sim$

$\pm 100$  G/s and then ramped to the negative direction from  $\sim 0$  G to  $-4000$  G, then back to  $\sim 0$  G at a rate of  $\sim \pm 100$  G/s. Data was acquired using National Instruments DAQ board and an automated Lab-VIEW data acquisition program.

#### 2.2.4 Kerr-effect Optical Microscopy

As one of several magneto-optical effects, Kerr-effect<sup>[41]</sup>, named after Joule Kerr, is the rotation of linearly polarized light when reflected from the magnetized sample surface. The plane-polarized electromagnetic light wave will interact with a magnetized material because of the Lorentz force. For the Kerr effect, there are two important amplitudes, the Kerr amplitude  $K$  and the normally reflected amplitude  $N$ , which can cause the rotation of the light.  $K$  is generated from the magnetic contribution. The contrast of the domains for a Kerr-Microscopy is caused by the ratio of  $K$  versus  $N$ .

There are several types of Kerr microscopy for different directions of magnetization. The longitudinal Kerr effect (Figure 2-6 (a) and (b)) occurs, when the Kerr rotation is proportion to the magnetization which is either parallel or perpendicular to the incident beam and the Kerr amplitude is polarized orthogonal to  $N$  and  $\vartheta \neq 0$ . In this case,  $K$  is proportional to the angle of incident beam with the  $z$  axis as  $K \propto \sin(\vartheta)$ . When  $\vartheta = 0$ , the effect is known as polar Kerr-effect, which is used to image the out-of-plane domains that are perpendicular to the surface.

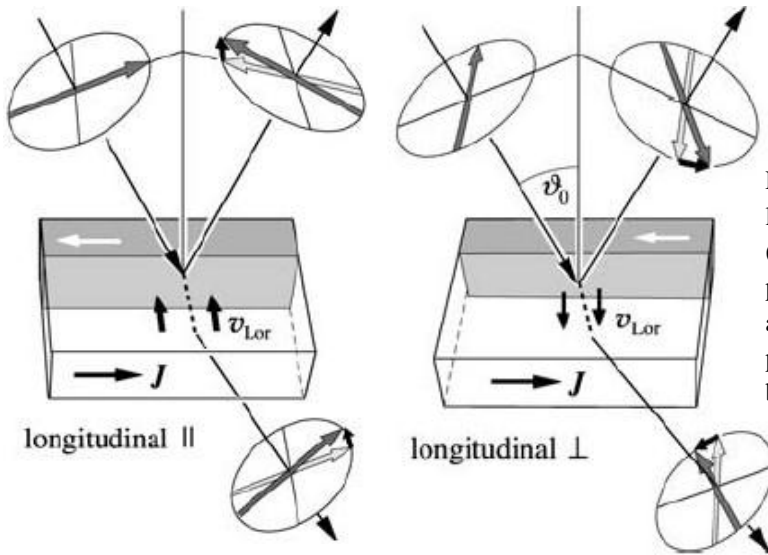


Figure 2-6 The scheme of longitudinal Kerr-effect, where (a) shows the Kerr rotation parallel to the incident beam and (b) shows the Kerr rotation perpendicular to the incident beam. Take from ref. [42]

The transverse Kerr-effect (Figure 2-7) happens when the magnetization is perpendicular to the plane of incidence. Only light with parallel polarization will generate a Kerr amplitude. It is also proportional to  $\sin(\vartheta)$ , but  $K$  is parallel to  $N$ .

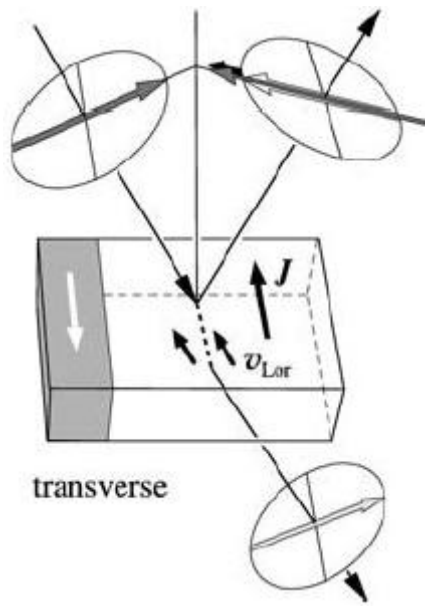


Figure 2-7 The scheme of transverse Kerr-effect, where magnetization is perpendicular to the plane of incident beam. Take from ref. [42]

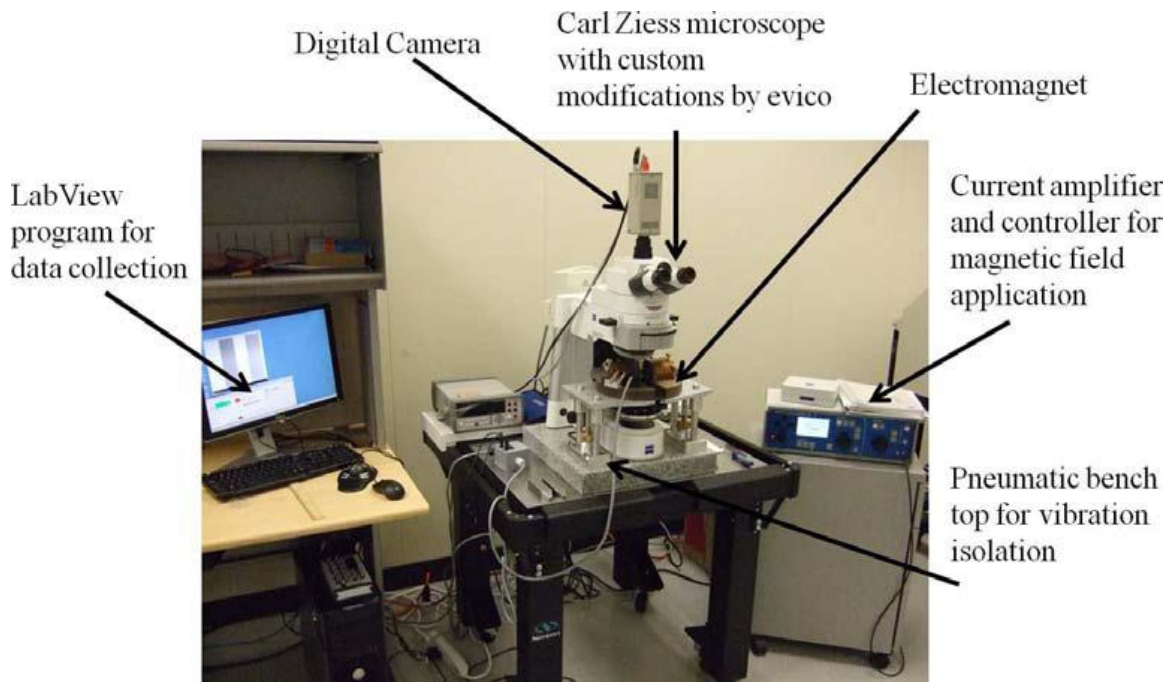


Figure 2-8 The wide field microscopy set ups. Taken from [30]

The Kerr Microscopy used in this thesis is the wide-field Kerr Microscopy which has been assembled by evico magnetics GmbH (Figure 2-8). Optical illumination is applied. The microscope has a range of imaging field from several mm down to hundreds of  $\mu\text{m}$  with different objective lenses from  $5\times$  to  $100\times$ . The electromagnet is capable to apply an inplane magnetic field up to 1 T. Both the sample stage and the electromagnet are rotatable. The whole system is controlled by a Lab-VIEW program. A CCD camera is used to obtain digital images. A background image processing is carried out to obtain better contrast.

To obtain a stress free sample surface for the imaging, the single crystal disks have been polished using increasingly finer SiC sheets down to 1200 grit size and followed by the alumina suspension down to  $0.3\ \mu\text{m}$ <sup>[42][44][45]</sup>. An additional more than 4 hours polishing was applied using colloidal amorphous silica<sup>[28][45]</sup> suspension. The polishing process is

similar to that described by Mudivarthi et al. <sup>[45]</sup>. It was found that to reveal the real domain structures, the polishing time for the iron-cobalt sample single crystal disks should be larger than for FeGa alloys, i.e., where 1-3 hours additional polishing with silica suspension could be enough to reveal the real domain structures, but at least 4 hours is essential. Due to the small sample size ( $\sim 0.51 \times 5.93^2 \text{mm}^3$ ), larger polishing time was needed here.

## Chapter 3 Results

VSM, Torque and domain images have been measured for four Iron-cobalt single crystal sample disks. Figure 3-1 to 3-13 show the measured results for one sample of the determination of the magnetic properties. The experimental results for the rest of samples are listed in Appendix 2. The results calculated from experiment data are summarized in table 3-1 to 3-4. The magneto-optical Kerr Microscopy images and discussion are displayed in Appendix 3.

The remarkable features of the data are:

- 1, easy magnetization direction is  $\langle 110 \rangle$ , agreeing with  $K_1 < 0$ ;
- 2, the anisotropy is changing from 2-fold (uniaxial) to 4-fold (cubic) as the measuring field is increased;
- 3, the magnetostriction is large;
- 4, the saturation magnetization is small compared to Permendur;
- 5, the saturation field is 2500 Oe (Oersted) for magnetization curves and 1500 Oe for magnetostriction;

### 3.1 Vibrating Sample Magnetometer Data

The VSM data was plotted by Origin 8.0 software. The magnetization and field units provided by the VSM (emu and Oe) were converted to emu/cc and G. Every set of data for the four sample disks were normalized to eliminate environmental influences.

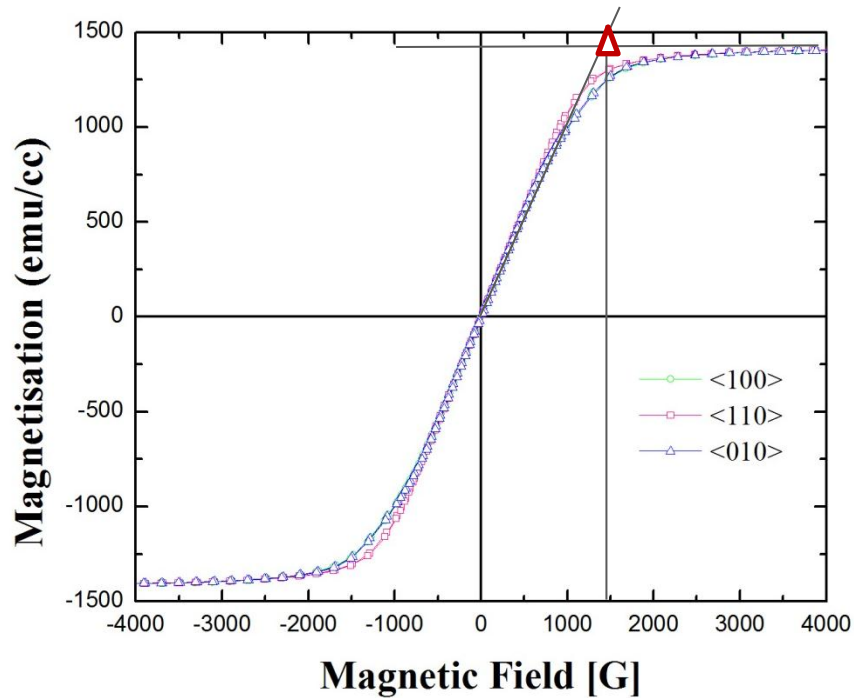


Figure 3-1 The magnetization curves of [n-001] single crystal sample 1-1 (refer to table 2-1) with magnetic field applied in different directions ( $\blacktriangle$  is point where the anisotropy field has been estimated)

Figures 3-1 show the VSM plot for sample disk 1-1 respectively. From the magnetization curves, we observed:

- 1, the  $\langle 110 \rangle$  direction is the easy direction of magnetization of disks with (100) normal.
- 2, the  $\langle 100 \rangle$  curve and  $\langle 010 \rangle$  curve almost superimpose with each other.
- 3, the samples are quite saturated with the magnitude of the applied field (2500Oe)
- 4, no hysteresis is found in all of three directions.
- 5, the saturation magnetization (1.8T) is relatively small when comparing it with Permendur (2.4T).

6, Close observation of the figures reveals that when applied field is along a hard direction, magnetization tends to go along easy direction up to a certain point and then breaks away from that and eventually going to saturation.

7, the observable area between the magnetization curves along  $\langle 100 \rangle$  and  $\langle 110 \rangle$  is very small.

8, the coercivity is very small (close to zero), as is shown in figure 3-2.

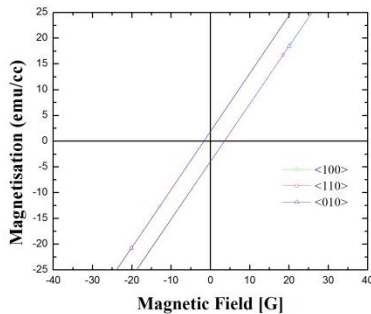


Figure 3-2 The coercivity of sample 1-1

Without applied field  $H$ , the direction of magnetization lies on the easy axes, which equivalent to an applied field and the value of which is called  $H_K$ , the anisotropy field. In magnetization curves,  $H_K$  can generally be determined by the saturation field along hard axis. In the case of  $\text{Fe}_{35}\text{Co}_{65}$  single crystal disks,  $H_K$  is estimated by extrapolated the linear part of magnetization curve to intersect with the line of saturation magnetization (as is shown in Figure 3-1). The results are listed in table 3-2.

As mentioned in Chapter 2, the magnetocrystalline anisotropy can be measured from the difference of area between the magnetization curves along different crystallographic directions. Table 3-3 listed all the calculated value of the anisotropy constant  $K_1$  from magnetization curves of sample 1-1 to 1-4.

### 3.2 Torque Magnetometer

The Torque data was plotted by Origin 8.0 software. The field data provided by the Torque magnetometer (dyne centimeter and Oe) was converted to Joule and G. To obtain the torque density ( $J/M^3$ ), the measured torque data was divided by the volume of the sample.

$$\text{Torque Density} = \frac{\text{Torque}}{\pi(D/2)^2 \cdot t} \quad (3-1)$$

where D is the diameter and t is the thickness of each specimen. The torque values were obtained at every  $5^\circ$  of the rotation of the applied field. Every set of data for the four sample disks was normalized to eliminate environment influences.

Figures 3-3 to 3-6 display the torque curves of sample disks 1-1, obtained at different external magnetic field. The  $0^\circ$  point was aligned to be the [110] easy axis. The bottom curve is rotated clockwise from  $0^\circ$ - $360^\circ$ , while the top curve is rotated counterclockwise from  $360^\circ$ - $0^\circ$ .

Figure 3-7 is the polar plot of sample disks 1-1, which shows the revolution of the anisotropy with the change of magnetization. It is very clear that as the magnetization increases from the lowest field to the highest field applied here, the symmetry of anisotropy changes from uniaxial anisotropy (2 fold) to cubic anisotropy (4 fold).

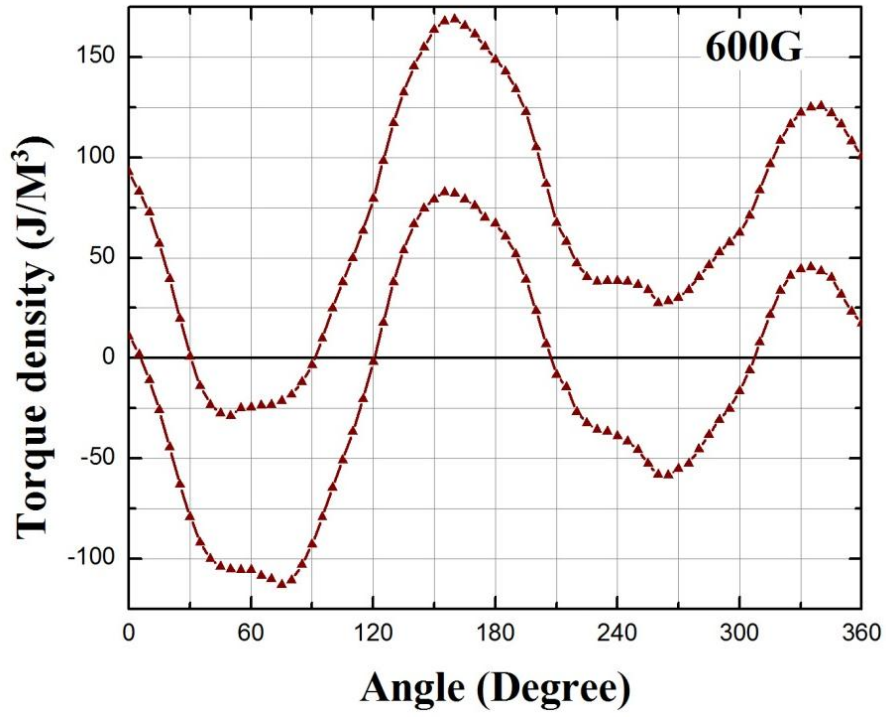


Figure 3-3 Torque curves of sample 1-1 at 600G

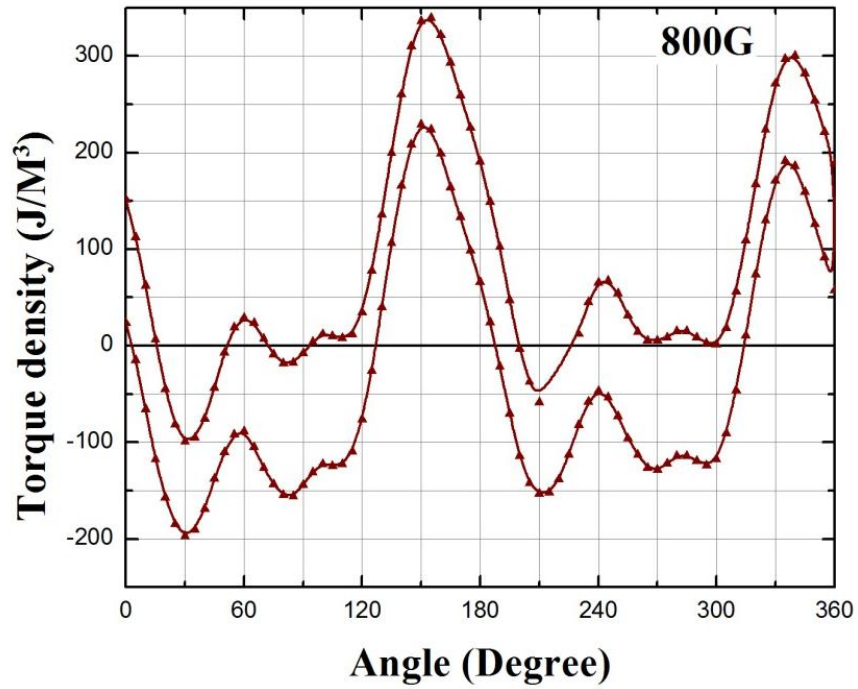


Figure 3-4 Torque curves of sample 1-1 at 800G

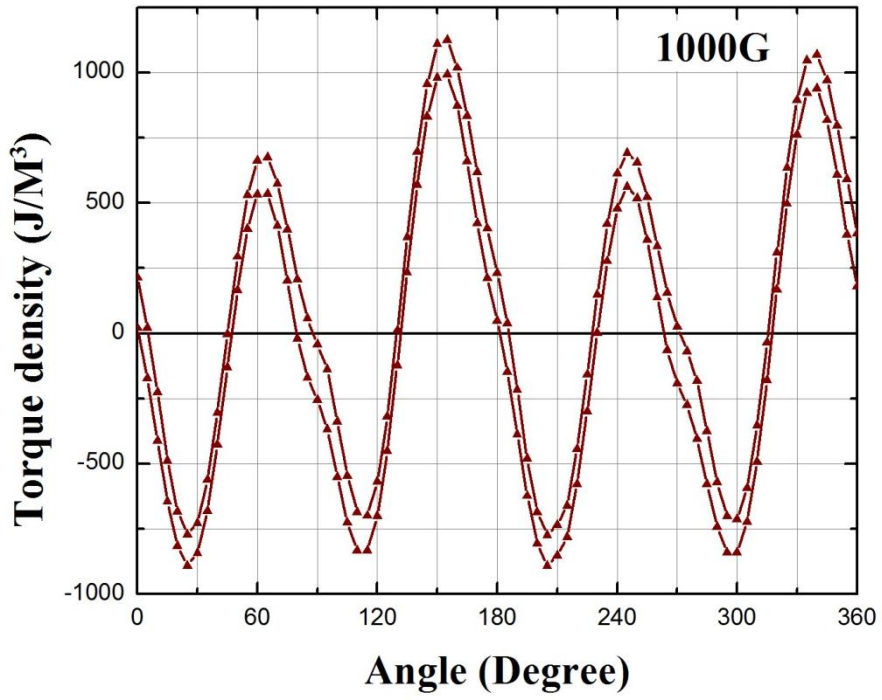


Figure 3-5 Torque curves of sample 1-1 at 1000G

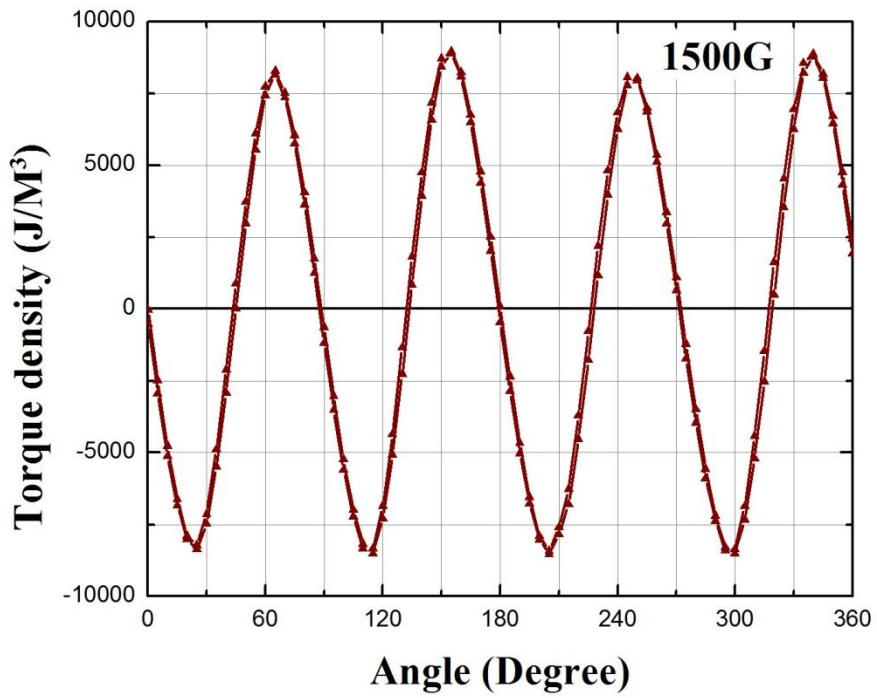


Figure 3-6 Torque curves of sample 1-1 at 1500G

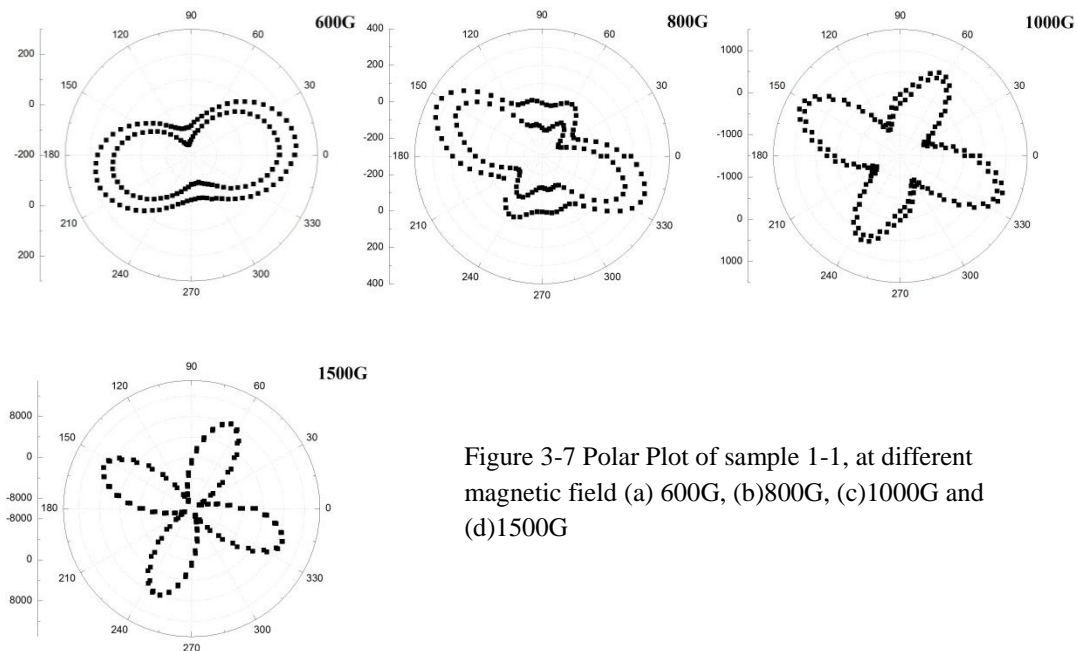


Figure 3-7 Polar Plot of sample 1-1, at different magnetic field (a) 600G, (b)800G, (c)1000G and (d)1500G

In Torque curves, when  $H=H_k$ , no rotational hysteresis should be found on the x axis. By integrating the y-axis normalized torque curves from low field to high field, the anisotropy field can be estimated at the field that the difference of area between the clockwise and counterclockwise rotated torque curves at the same field reaching its minimal ( $\approx 0$ ). The integration was done with the help of Origin 8.0 software. The experimentally obtained rotational hysteresis data is listed in table 3.1 and the estimated values of  $H_k$  are listed in table 3.2.

Sample Name	Difference of Area (G)			
	1-1	1-2	1-3	1-4
600	44.6888	20.16235	20.91296	--
800	21.8409	1.488585	4.632037	17.50299

1000	1.5331	0.876306	--	1.419749
1200	--	--	7.778456	-13.6797
1500	0.0724	0.217806	--	--
1600	--	4.505146	--	--
1700	--	--	0.44014	0.331475

Table 3.1 Rotational hysteresis presented by the difference of area of sample 1-1 to 1-4

Sample name	$H_k^*$ (G)	$H_k^{**}$ (G)	$H_s(G)^{***}$	$H_s^*$ (G)
1-1	1490	1500	1500	2500
1-2	1400	1500	1500	2500
1-3	1700	1700	1400	2500
1-4	1600	1700	1500	2500
FeGa <sub>20</sub>	1083 <sup>[36]</sup>		1000 <sup>[30]</sup>	

Table 3.2 Anisotropy field and saturation field of magnetostriction for sample 1-1 to 1-4

\*obtained from Magnetization curves; \*\* obtained from Torque curves; \*\*\* saturation field of magnetostriction obtained from magnetostriction curves

From observation, the symmetry of torque curves changes from  $l = 2$  to  $l = 4$ . Thus, we can assume that two types of anisotropy exist: one is uniaxial ( $l = 2$ ), and the other is cubic ( $l = 4$ ).

$$E_{total} = E_{uni} + E_{cub} \quad (3-1)$$

$$E_{uni} = K_{u0} + K_{u1} \sin^2 \theta_M + \dots \quad (3-2)$$

$$E_{cub} = K_{0c} + K_1(\alpha_1^2 \alpha_2^2 + \alpha_2^2 \alpha_3^2 + \alpha_3^2 \alpha_1^2) + K_2 \alpha_1^2 \alpha_2^2 \alpha_3^2 + \dots$$

For the (001) sample disk:

$\alpha_1 = \cos \varphi$ ;  $\alpha_2 = \sin \varphi$ ;  $\alpha_3 = 0$ . ( $\varphi = \theta_M$ , as the easy axis is the reference direction.)

$$E_{cub} = \frac{1}{4} K_1 \sin^2(2\theta_M)$$

$$\text{The torque } T = -\frac{\partial(E_{uni} + E_{cub})}{\partial\theta_M} = -\left[\frac{1}{2} K_{u1} \sin(2\theta_M) + \frac{1}{2} K_1 \sin(4\theta_M)\right] \quad (3-3)$$

The cubic anisotropy constant  $K_1$  and the uniaxial anisotropy constant  $K_{u1}$  were calculated by a sum of sine fitting analysis of the torque curves obtained at field  $H = H_k$ , using Matlab 7.9.0 program with following model:

$$T(x) = T_2 * \sin(2 * x + c_1) + T_4 * \sin(4 * x + c_2)$$

The confidence limit of the fit is larger than 0.98 for all samples (close to one), which indicates most of data points were counted in this model.  $\frac{1}{2} K_{u1} = -T_2$  and  $\frac{1}{2} K_1 = -T_4$ .

The values of  $K_1$  and  $K_{u1}$  are shown in table 3.3.

Sample name	Saturation Magnetization(emu/cc) <sup>***</sup>	$K_1^*$ (J/M <sup>3</sup> )	$K_{u1}^{**}$ (J/M <sup>3</sup> )	$K_1^{**}$ (J/M <sup>3</sup> )
1-1	1437	$-2.16 \times 10^4$	$-1.22 \times 10^3$	$-1.64 \times 10^4$
1-2	1256	$-2.38 \times 10^4$	$-1.98 \times 10^3$	$-1.82 \times 10^4$
1-3	1341	$-1.69 \times 10^4$	$-1.29 \times 10^3$	$-1.57 \times 10^4$
1-4	1647	$-6.06 \times 10^3$	$-1.88 \times 10^3$	$-1.29 \times 10^4$
FeGa <sub>20</sub>		$3.23 \times 10^{2[36]}$		

Table 3.3 Anisotropy field and constants of single crystal Fe<sub>35</sub>Co<sub>65</sub> samples

\*obtained from Magnetization curves; \*\* obtained from Torque curves

\*\*\* error exist in measurement of polished sample volume (some of them may be unflatten)

### 3.3 Magnetostriction

Figure 3-8 shows the magnetostriction data for sample 1-1 obtained using an automated Lab-VIEW data acquisition program. Throughout this thesis,  $\lambda_j^i$  means the magnetostrictive strain along  $\hat{j}$  direction, when field applied along  $\hat{i}$  direction.

a, b and c represent the fraction of magnetic moments oriented along  $\hat{x}$ ,  $\hat{y}$  and  $\hat{z}$  respectively. In a perfectly demagnetized sample and in the absence of any residual stress,  $\lambda_x^x$  and  $\lambda_y^y$  are always  $2/3\lambda$ , meaning the remanent states  $a = b = c = 1/3$ . However, this is not the case in all the samples. Since the hysteresis in the magnetostriction data is almost negligible, the deviation can be attributed to some anisotropy, may possibly due to the presence of a residual stress. It is notable that more hysteresis of magnetostriction observed along [110] direction (Figure 3-9) than that along [100] direction.

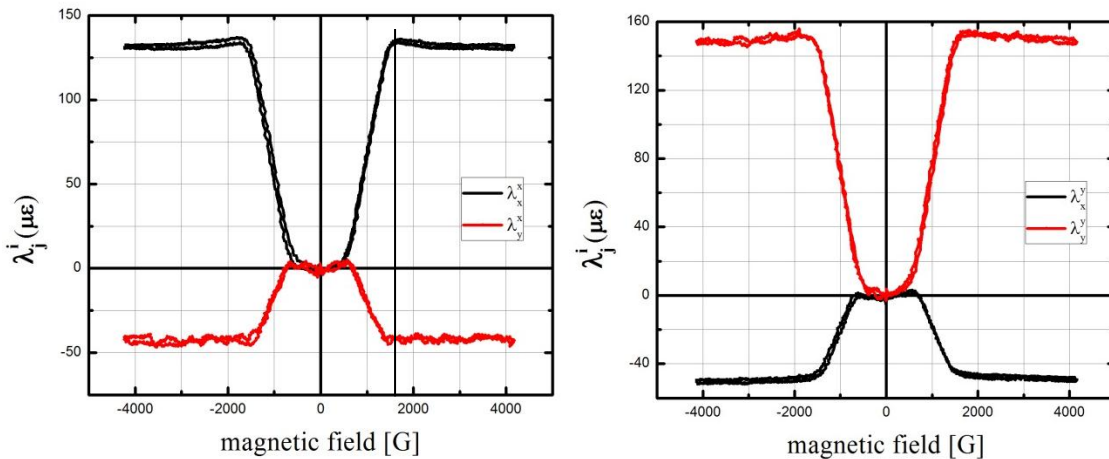


Figure 3-8 Magnetostriction of sample 1-1 under H field applied along  $\hat{x}$  (left) and  $\hat{y}$  (right)

Solid line in the left plot indicates the saturation field of the magnetostriction curves

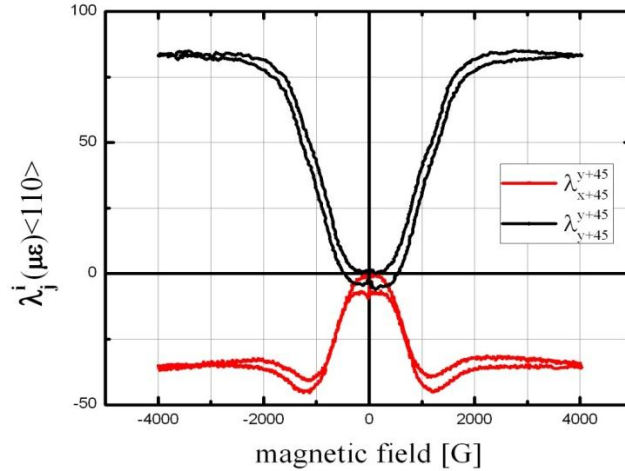


Figure 3-9 Magnetostriction of <110> direction of sample 1-3 under H field applied along <110> direction

The values for  $\lambda_x^x$ ,  $\lambda_y^y$ ,  $\lambda_x^y$ ,  $\lambda_y^x$  and  $\lambda_{100}$  are given in table 3.1. The measured  $\lambda_{100}$  is 23% larger than  $\lambda_{100}$  data of Permendur listed in table 1.1<sup>[8]</sup>. From table 3.1,  $\lambda_{100}$  is almost 34% larger than  $\lambda_{110}$ . The magnetostriction along [110] direction is the projection of magnetostriction of [100] and [111]. In FeCo alloys,  $\lambda_{100} \gg \lambda_{111}$ <sup>[35]</sup>, leading to the lower value of  $\lambda_{110}$ .

Sample	$\lambda_x^x$	$\lambda_y^y$	$\lambda_x^y$	$\lambda_y^x$	$\lambda_{100}$
1-1(300 °C)	137±1	-46±1	-51±1	155±1	194.5±2
1-2(875 °C)	105±1	-63±1	-67±1	121±1	178±2
1-3(790 °C)	128±1	-60±1	-59±1	130±1	188.5±2
1-3(<110>)	--	--	--	--	$\lambda_{110}$ :125±2
1-4(690 °C)	98±1	-61±1	-67±1	124±1	175±2

Table 3.4 Magnetostriction at H=4000G

## Chapter 4 Discussion

The high value of  $\lambda_{100}$  can be explained by the existence of a second phase. The value of  $\lambda_{100}$  is high and agrees with the results reported Dai and Wuttig<sup>[27]</sup>. Four sample disks (1-1 to 1-4) are annealed at different temperature, 300°C, 875°C, 790°C and 690°C respectively. From the partial phase diagram (Figure 2-2), the bcc// (bcc+fcc) phase boundary of Fe<sub>35</sub>Co<sub>65</sub> alloy is located at 915°C. According to this expectation, the magnetostriction will increase with increased annealing temperature of the four sample disks and will reach to its maximum in sample 1-2 (highest annealing temperature near the phase boundary). However, experimental data (Table 3.4) show that similarly high values of  $\lambda_{100}$  exist in all four samples and do not depend strongly on their annealing temperature. Since the single crystal had been annealed at 860°C for one week and slow cooled thereafter, the microstructure was likely little affected by the subsequent anneals. A second phase may have already been formed during the first long anneal. The additional annealing performed in this study (63hrs, 0.3 hrs, 0.8hrs and 1hrs for sample 1-1 to 1-4 respectively), did not alter the initial microstructure substantially.

The contribution of the magnetostriction to the anisotropy is significant. Two kinds of anisotropy energies exist in a ferromagnetic crystal: the magnetocrystalline anisotropy,  $K_1$ <sup>[43]</sup> and the magnetoelastic anisotropy,  $K_{me}$ <sup>[43]</sup>. If the axis of stress,  $\sigma$ , is fixed, the energy changes as the magnetization rotates. Thus, the magnetoelastic anisotropy ( $K_{me} \propto (C' \lambda_{100}^2 + 2C_{44} \lambda_{111}^2)$ ) is produced. It is known that for Ni<sup>[42]</sup> ( $\lambda_{100} \approx 45.9$ ppm,  $\lambda_{111} \approx 24.3$ ppm),  $K_{me} \approx 0.02K_1$ , i.e.,  $K_{Me} \ll K_1$ . However, in FeCo alloys  $\lambda_{100} \gg \lambda_{111}$ <sup>[35]</sup>,  $K_{me} = \frac{9}{4} c' \lambda_{100}^2$ , meaning that for the presented alloys,  $\lambda_{100} \approx 200$  ppm, the magnetoelastic

contribution,  $K_{me} \approx 0.1K_1$ , is significant. Thus, the value of anisotropy constant will be influenced by their magnetoelastic energy.

Comparison between magnetostriction curves and torque density curves shows that the second phase contributed to the increase of the magnetostriction. At very low field, the anisotropy is very small and uniaxial ( $T_2$ ). With increasing magnetic field, a second peak becomes more prominent and changes the torque curves to four-fold symmetry ( $T_4$ ). The evolution of the torque amplitude should be compared with the evolution of magnetostriction curves as a function of applied field. This comparison is shown in figure 4-1. It can be seen that the magnetostrictive elongation begins at low fields and saturation is reached around the estimated anisotropy field. Torque density curves at different magnetic field have been fitted with the help of Matlab 7.9.0 software to quantify the evolution of the torque symmetry changing with field. The torque  $T(\theta) = T_2 * \sin(2*\theta + c_1) + T_4 * \sin(4*\theta + c_2)$  has been used to determine the amplitude of the two and four fold symmetry  $T_2$  and  $T_4$ . The confidence limit of the fit is larger than 0.90 except for the curves obtained at 500 Oe (0.8025).

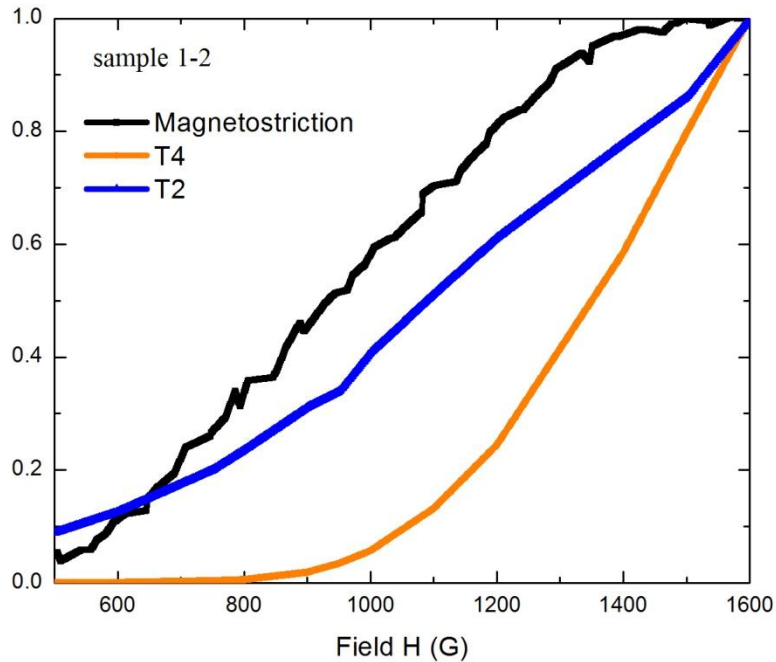


Figure 4-1 Comparison between the amplitude of T<sub>2</sub> and T<sub>4</sub> vs field and the magnetostriction vs field

When comparing the slope of T<sub>2</sub>, T<sub>4</sub> with the magnetostriction in Figure 4-1, it becomes clear that T<sub>2</sub> evolves as a function of the external field as the magnetostriction does.

At high fields, the torque displays four-fold symmetry, with an easy axis (defined here as the direction along which the minimal of energy can be observed) of [110], which agrees with the magnetization curves. At low fields, the torque displays two-fold symmetry, with the torque curves at 600 Oe showing that the easy axis is [100]. From the magnetostriction measurements, the [100] direction has almost 30% higher magnetostriction than the [110] direction (refer to table 3.4). However, in a cubic crystal, there are four equivalent directions of [100] on the [001] plane. Thus, without another four-fold symmetry showing in the torque curves, it is reasonable to assume that the [100]

easy uniaxial second phase contributed to the larger magnetostriction along [100] direction. Figure 4-2 shows this change of the easy axis from  $\langle 100 \rangle$  (red arrow) to  $\langle 110 \rangle$  (blue arrow) the revolution of torque curves corresponds to magnetic field, with the two red triangles at  $90^\circ$  and  $135^\circ$ , showing the easy axis for the two fold and four fold symmetry of torque curves respectively.

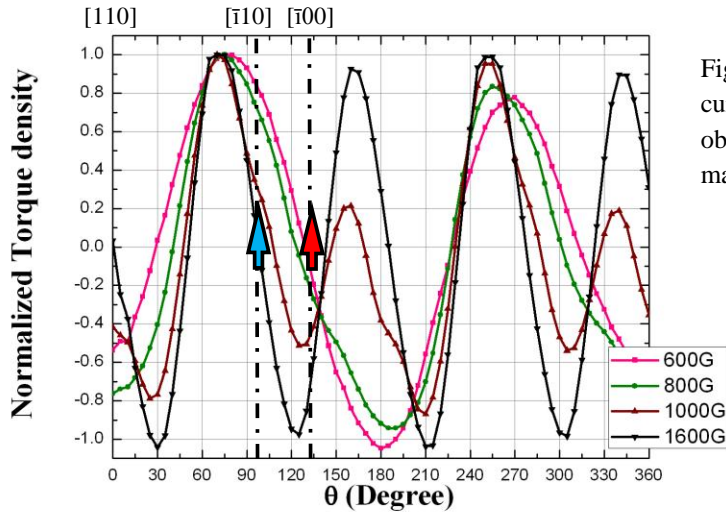


Figure 4-2, Normalized torque curves  $T(\theta)$  of sample 1-2 obtained at four increasing magnetic fields

The symmetry change of torque curves with increasing magnetic fields indicates that the second phase is symmetry related to the host.

As mentioned before, the easy axis can be determined by closely observing the torque curves obtained at different fields (figure 4-2). Initially  $T_2$  is shifted by 45 degrees with respect to  $T_4$  ([100] easy axis). At large fields it aligns with the easy direction ([110] easy axis).

According to the phase diagram, the second phase is most likely a FCC phase.

Considering both the changes of torque symmetry and the crystallographic properties of FCC and BCC structures, it is likely that the second phase consist of an epitaxial-fcc

precipitate, sharing a (110) common plane with the bcc host structure. As the external field increases, the magnetization of the FCC second phase aligns as with respect to the [110] easy direction (easy axis of four-fold symmetry) of the host. This is illustrated in figure 4-3 which shows how the symmetry of the magnetization changes as the magnetization of the uniaxial (tetragonal) fcc precipitate rotates into the [110] easy direction of the host.

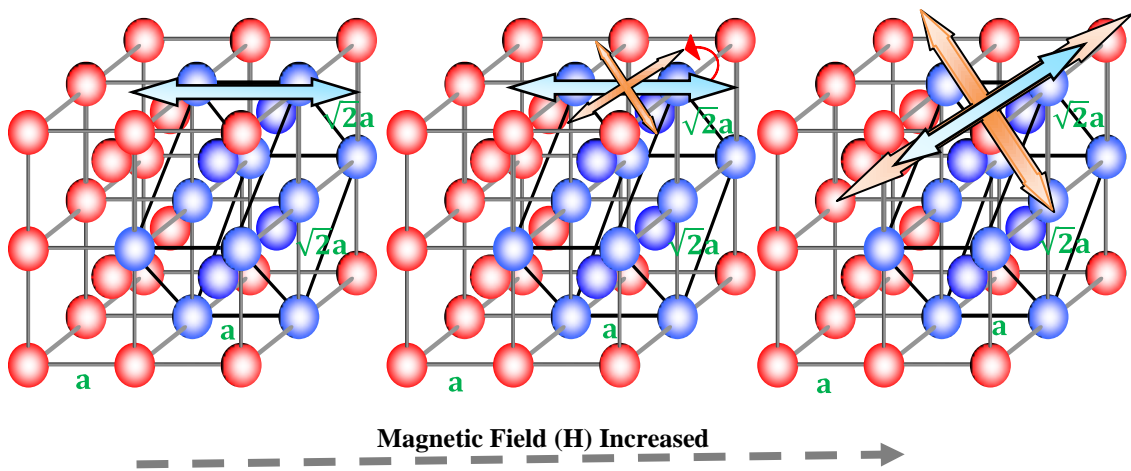


Figure 4-3 Symmetry of the presented crystal, where the red balls form the host with a bcc structure and the blue balls form the coherent fcc second phase. The easy directions of the precipitates and the host displays in blue and orange arrows respectively.

The saturation magnetization of the  $\text{Fe}_{35}\text{Co}_{65}$  alloy investigated in this study is significantly lower than the values in the literature <sup>[8]</sup> indicate. As mentioned in chapter 3, the saturation magnetization of the presented samples equals approximately 1.9 T (sample 1-1). According to the saturation magnetization data available from the literature <sup>[8]</sup>, it should be nearly 2.2 T for  $\text{Fe}_{35}\text{Co}_{65}$  alloys, i.e., 17% higher than the measured data. The existence of a second phase may explain this apparent discrepancy; the Fe-Co phase with a FCC structure processes a low spontaneous magnetization. Assuming that the concentration of cobalt in the precipitate is 0.95, i.e., one iron atom takes the face center

position and cobalt atoms take the rest positions in one unit cell, and assuming that Fe<sub>50</sub>Co<sub>50</sub> composition exists in the host, the percentage  $x$  of precipitates can be calculated as follows:

$$0.95x + 0.5(1 - x) = 0.65;$$

thus,  $x \approx 0.33$ .

Using the saturation magnetization of Fe<sub>5</sub>Co<sub>95</sub> alloys<sup>[8]</sup>, 1.7T, and the saturation magnetization of Permendur<sup>[8]</sup>, 2.3T, the percentage  $x$  of precipitates can be calculated as follows:

$$1.7x + 2.3(1 - x) = 1.875;$$

thus,  $x \approx 0.29$ . It can be seen that the calculated values percentage  $x$  from crystallographic symmetry and the saturation magnetization agree with each other.

The low susceptibility is unusual for FeCo alloys. For rotational magnetization the susceptibility is depending on the following relationship<sup>[43]</sup>:

$$\chi = \chi_0 \frac{I_s}{\sqrt{K}} \quad (4-7)$$

where,  $I_s = 1437 \text{ emu/cc}$ ;  $I_s^* = 1750 \text{ emu/cc}$ ;

$$K = K_1 + K_{Me} = K_1 + \frac{9}{4} \lambda_{100}^2 C' \times 10^{-1} = (2.16 \times 10^4 + 1.98 \times 10^3)(J/M^3) = 2.36 \times 10^4 (J/M^3) ;$$

$$K^* = K_1^* + K_{Me}^* = K_1^* + \frac{9}{4} \lambda_{100}^{*2} C'^* \times 10^{-1} = (0 + 1.11 \times 10^3)(J/M^3) = 1.11 \times 10^3 (J/M^3)$$

$\chi_0$  is a constant;  $\chi^* = 9$ ;

\* refers to the values of Permendur [8];

The values of  $C'$  and  $C'^*$  were taken from reference [46].

Thus, the susceptibility of the presented FeCo alloy can be calculated by using that:

$$\chi = \chi^* \cdot \frac{I_s}{\sqrt{K}} \cdot \frac{\sqrt{K^*}}{I_s^*} \approx 1.603$$

The susceptibility  $\chi$  is in more than 5 fold smaller comparing to Permendur. Thus, it is very reasonable for us to expect a second phase existing in the presented FeCo alloy.

## Chapter 5 Conclusion and future work

In conclusion, the Fe<sub>35</sub>Co<sub>65</sub> single crystal sample has been annealed by a long time at temperature (860°C) close to its fcc-bcc phase boundary to obtain the single crystal. Its magnetostriction constant  $\lambda_{100}$  is as high as 200ppm which is 23% higher than the measured value<sup>[8]</sup> of permendur (150ppm). The magnetocrystalline anisotropy constant  $K_1$  is in 5 fold smaller than that of permendur. The symmetry of torque curves changed from 2-fold to 4-fold as the external magnetic field increased, which indicates the existence of a second phase. It is proposed that the second phase is an epitaxial fct precipitate. Its lower saturation magnetization and the crystalline structures agree with each other semi-quantitatively. The torque data are interpreted by the alignment of the magnetization of the epitaxial fct precipitate in the bcc host by external field. The susceptibility,  $\chi \approx 1.63$ , is more than 5 fold smaller comparing to Permendur. The high magnetostriction is caused by the rotation of magnetization in the second phase.

Following features, if investigated in future, will be able to establish more explicit by the nature of the presented alloy and lead to other groups of high magnetostrictive alloys:

The crystal and domain structures of these Fe<sub>35</sub>Co<sub>65</sub> single crystals should be investigated further using Lorentz- and high resolution- Transmission Electronic Microscopy (LTEM+HRTEM) to identify the nanoscopic process leading to the high magnetostriction.

The domain structures should be investigated further using Magneto Optical Kerr Effect Microscopy with larger Fe<sub>35</sub>Co<sub>65</sub> single crystal samples (both in diameter and thickness).

Large samples will facilitate the polishing process to reveal the true domains helping to explain the magnetic anisotropic properties of the alloy.

The M-H curves can be investigated further as a function of the temperature (above Curie temperature of this material) using Vibration Sample Magnetometer. This will help to explain the low saturation magnetisation of these samples. If small amounts of fcc phases exist, a break in the M(T) curve will occur.

## Appendix 1: Result Figures (sample1-2 to 1-4)

### Appendix 1.1 Magnetization Curves

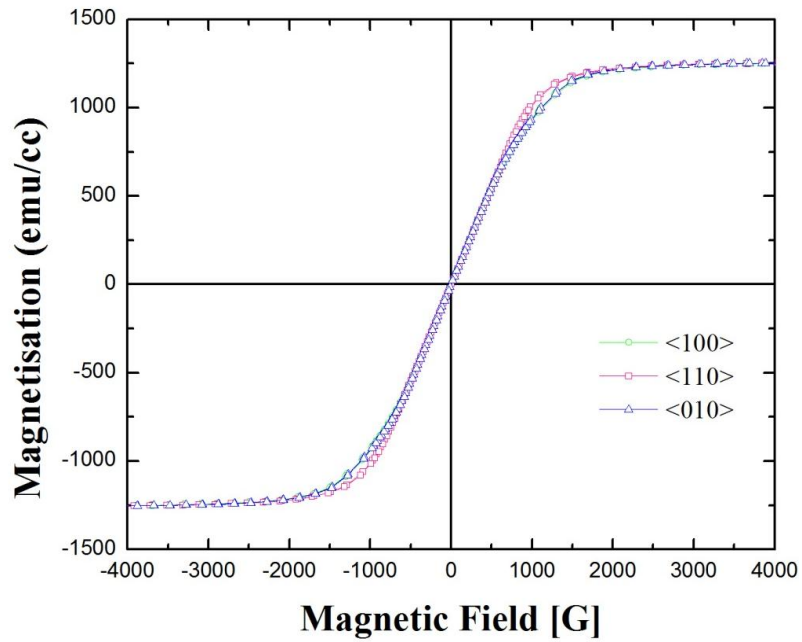


Figure a1-1 The magnetization curves of [n-001] single crystal sample 1-2 (refer to table 2-1) with magnetic field applied in different directions

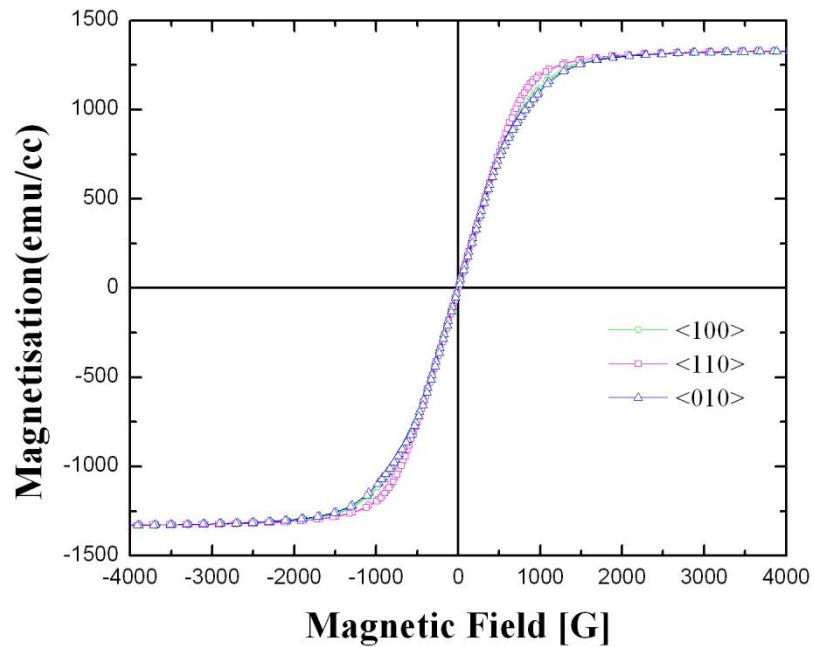


Figure a1-2 The magnetization curves of [n-001] single crystal sample 1-3 (refer to table 2-1) with magnetic field applied in different directions

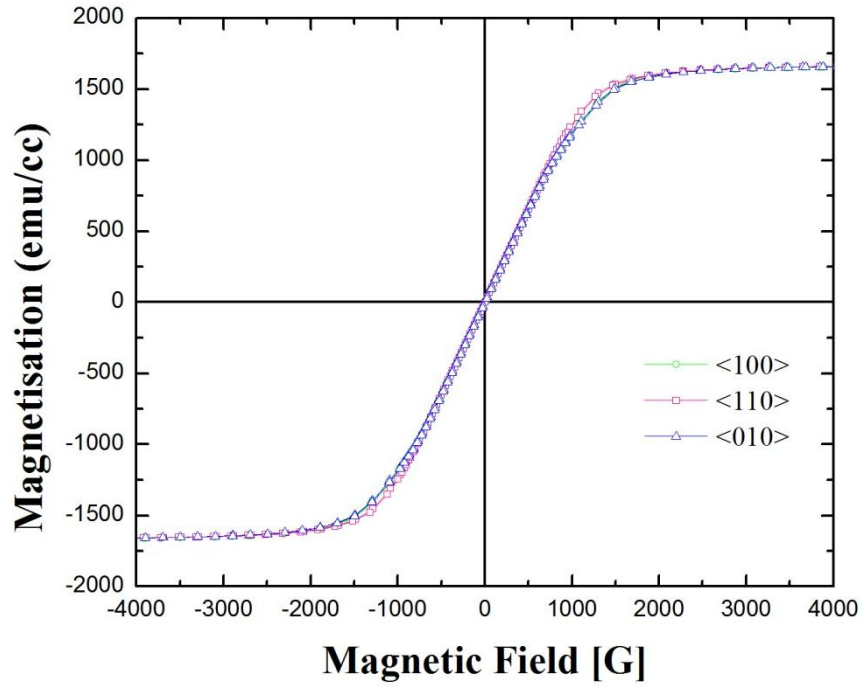


Figure a1-3 The magnetization curves of [n-001] single crystal sample 1-4 (refer to table 2-1) with magnetic field applied in different directions

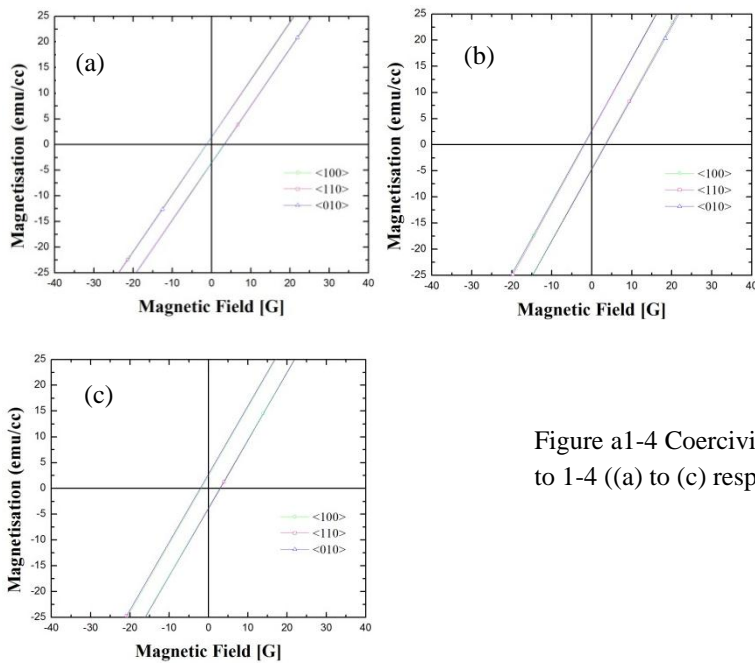


Figure a1-4 Coercivity of sample 1-2 to 1-4 ((a) to (c) respectively)

Appendix 1.2 Results from Torque Measurements

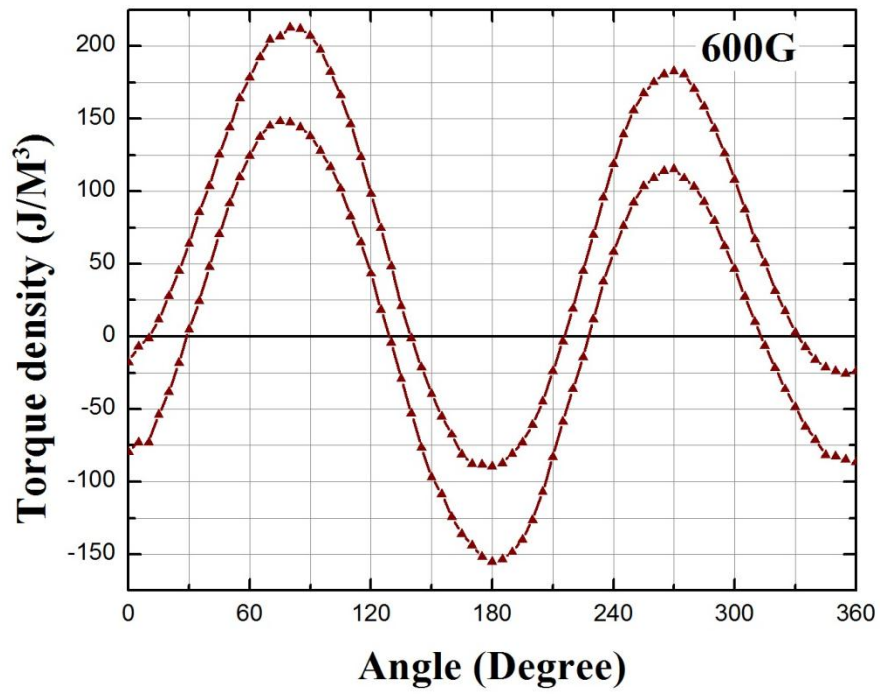


Figure a1-5 Torque curve of sample 1-2 obtained at 600G

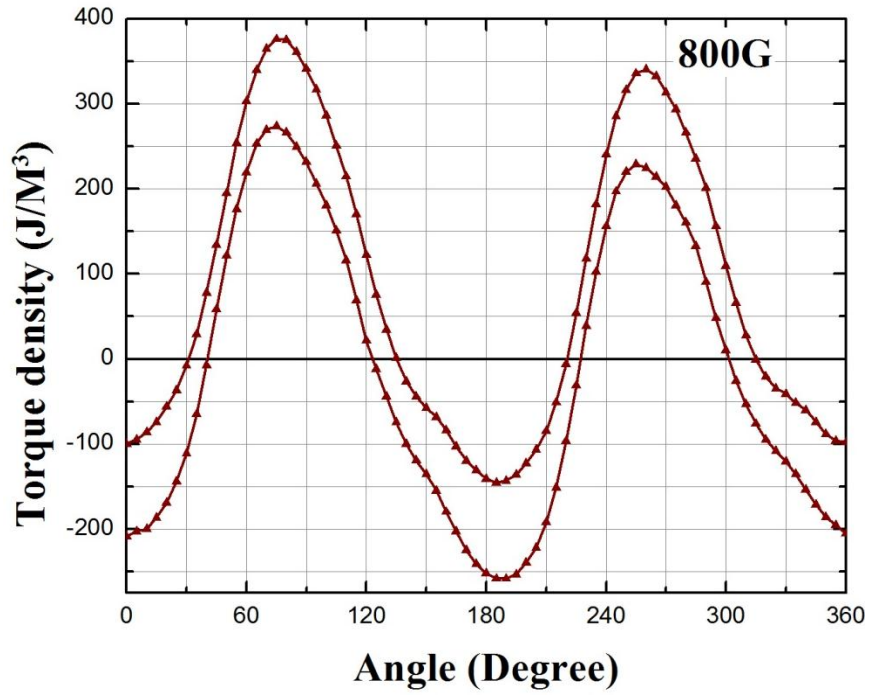


Figure a1-6 Torque curve obtained of sample 1-2 at 800G

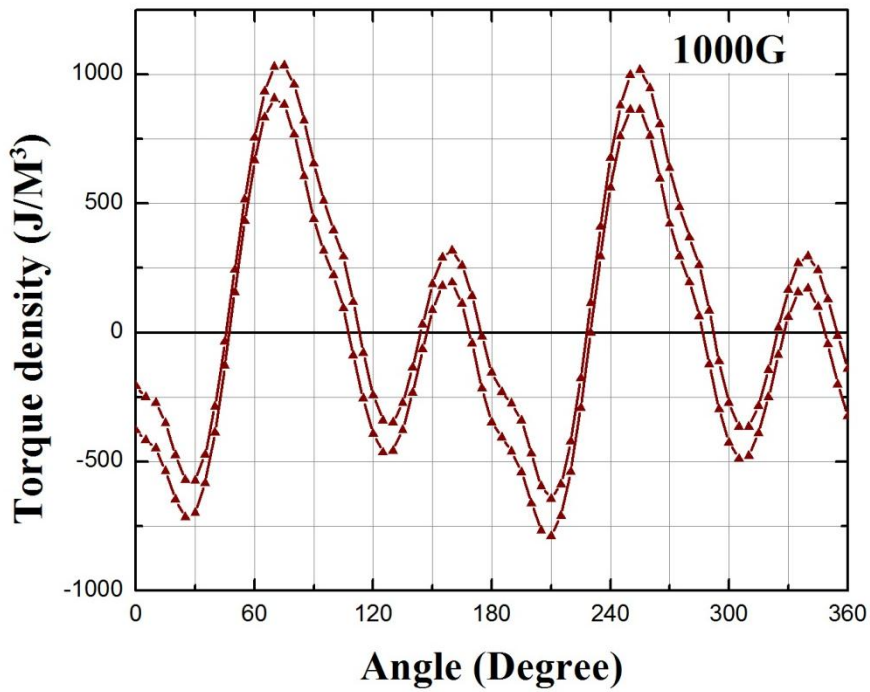


Figure a1-7 Torque curve of sample 1-2 at 1000G

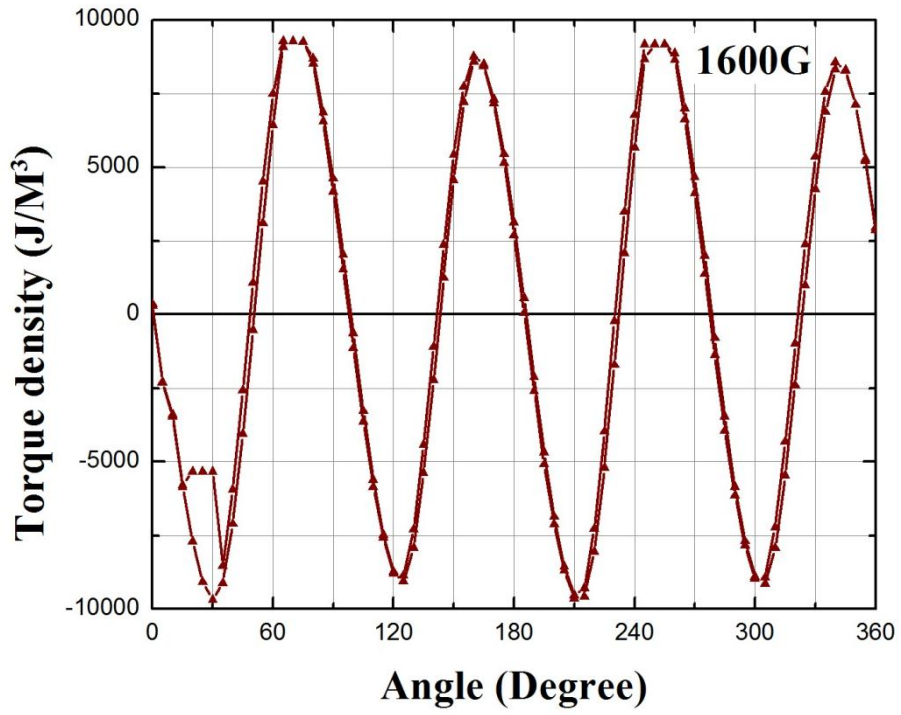


Figure a1-8 Torque curve of sample 1-2 obtained at 1600G

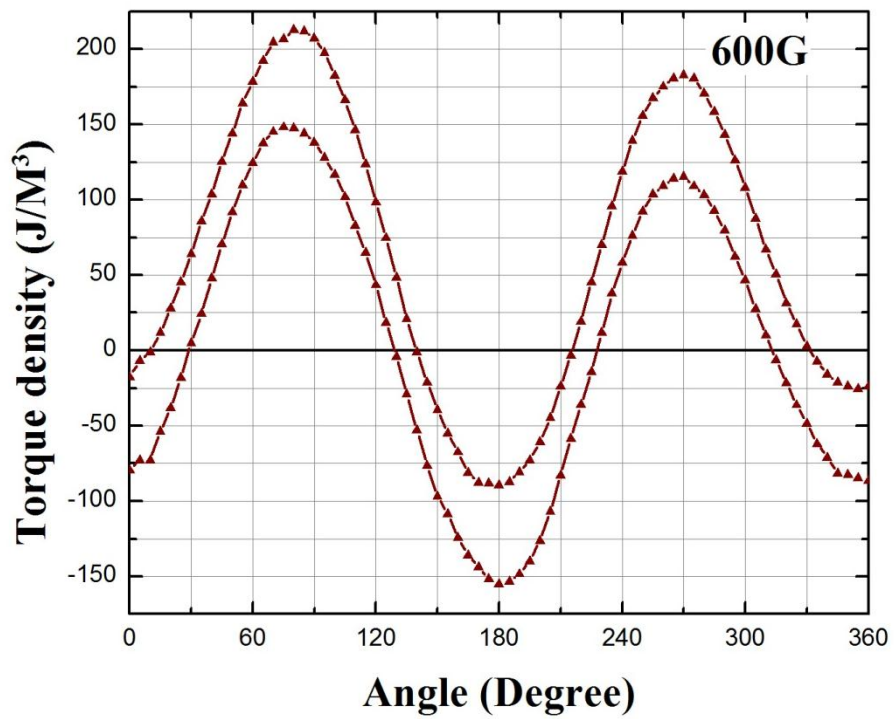


Figure a1-9 Torque curve of sample 1-3 obtained at 600G

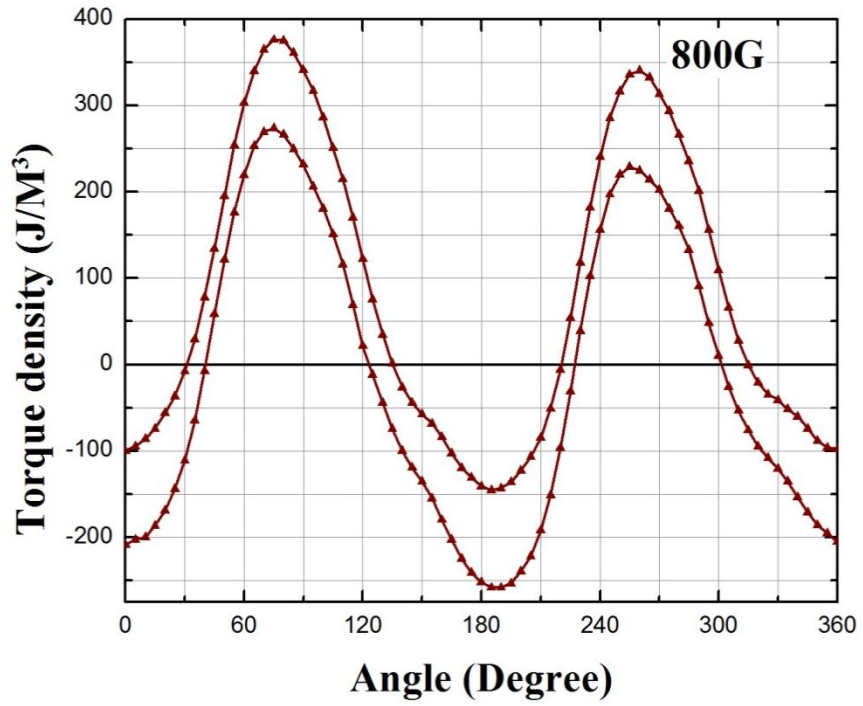


Figure a1-10 Torque curve of sample 1-3 obtained at 800G

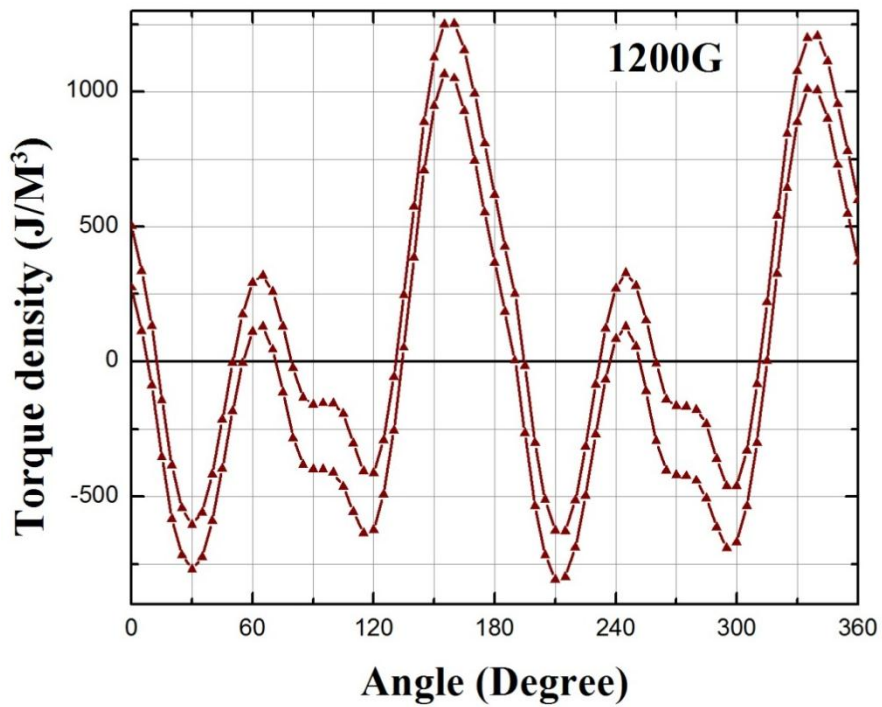


Figure a1-11 Torque curve of sample 1-3 obtained at 1200G

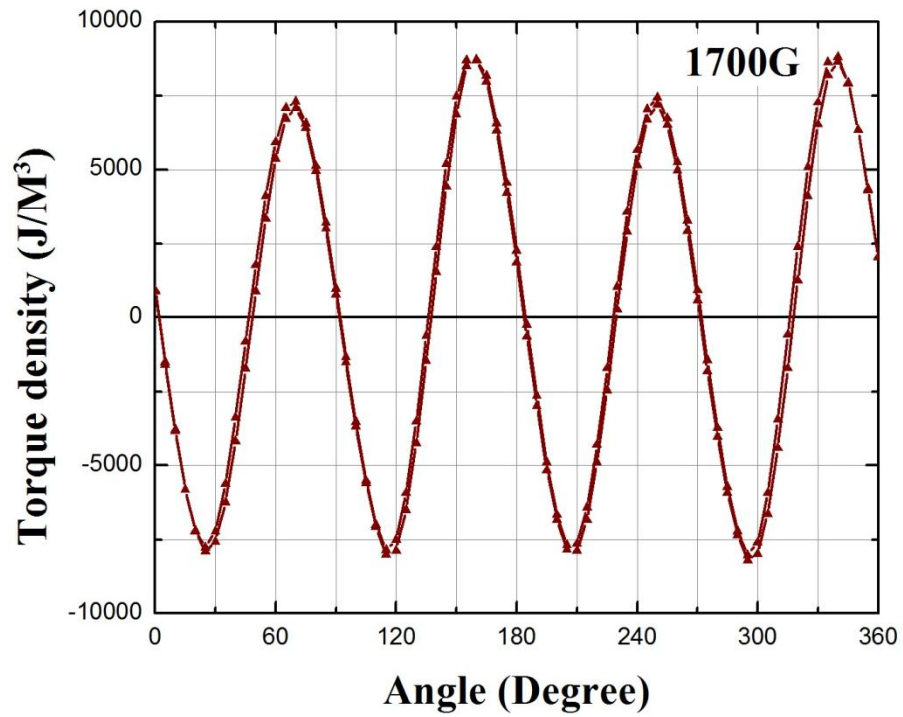


Figure a1-12 Torque curve of sample 1-3 obtained at 1700G

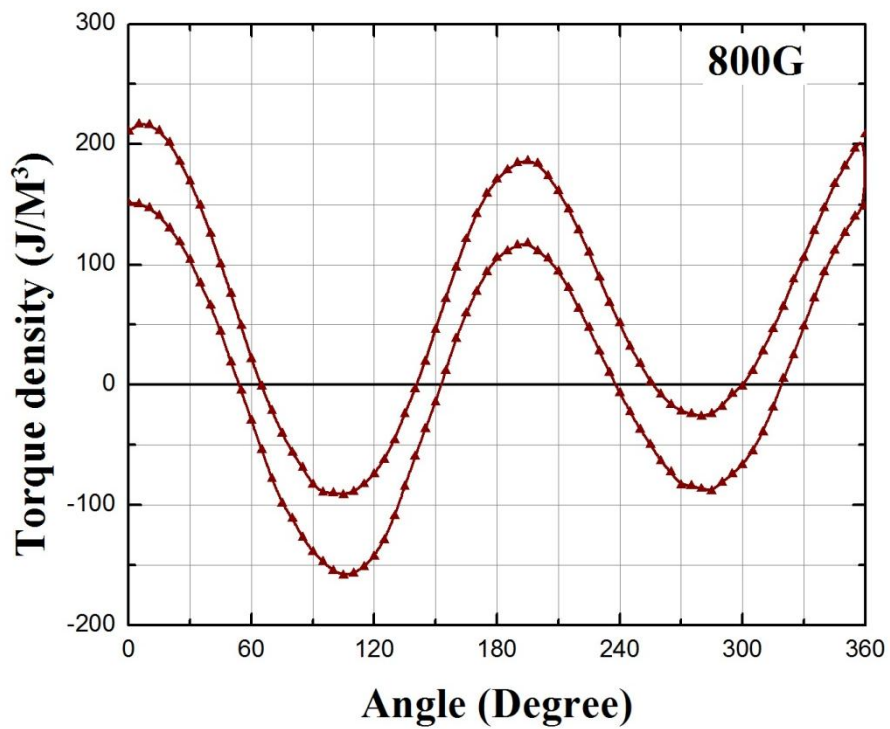


Figure a1-13 Torque curve of sample 1-4 obtained at 800G

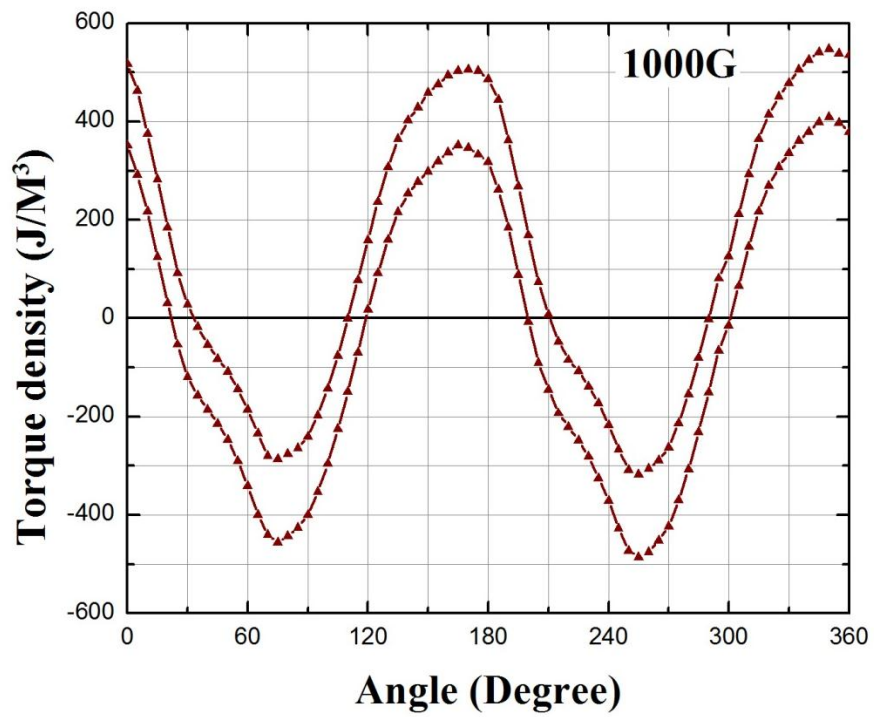


Figure a1-14 Torque curve of sample 1-4 obtained at 1000G

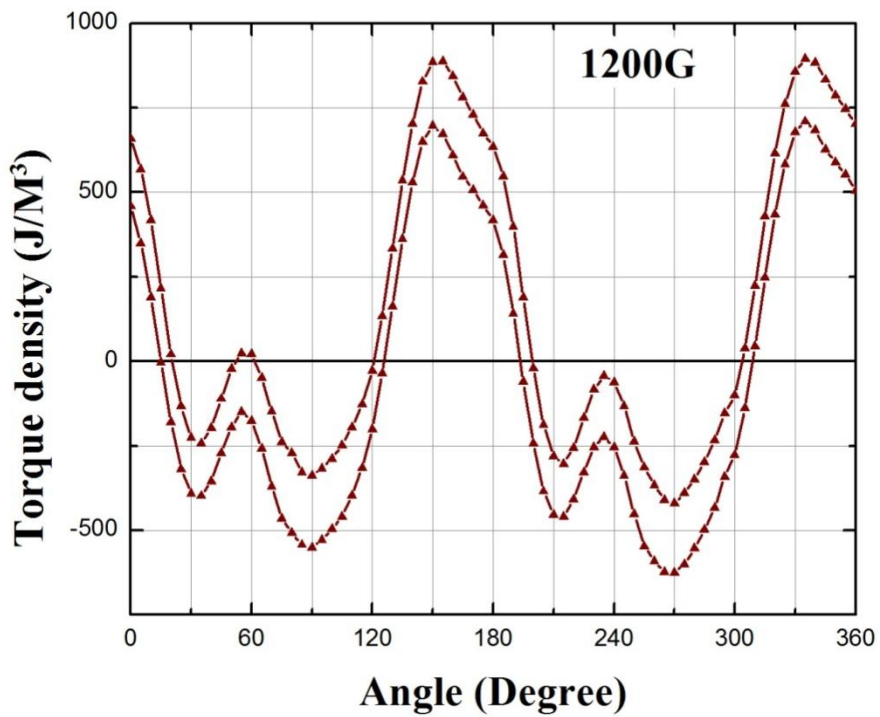


Figure a1-15 Torque curve of sample 1-4 obtained at 1200G

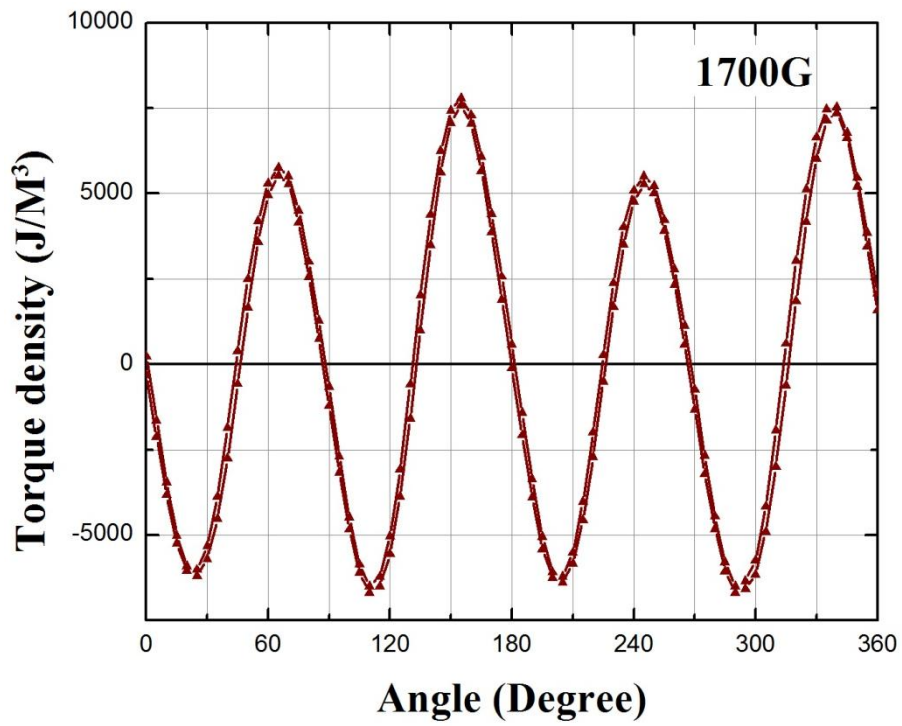


Figure a1-16 Torque curve of sample 1-4 obtained at 1700G

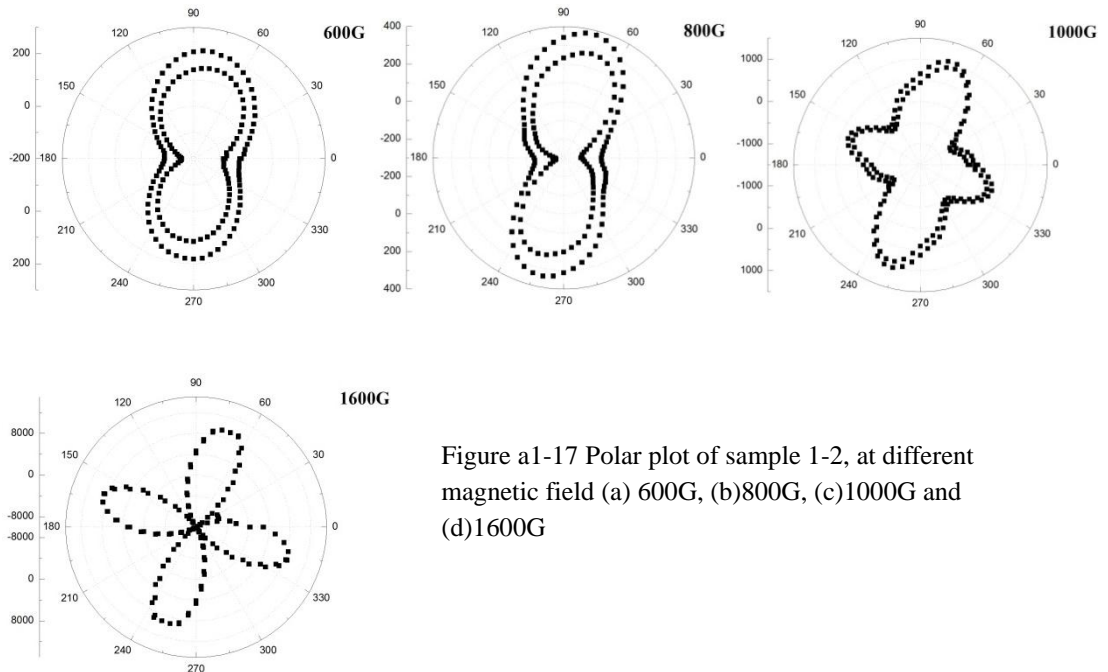


Figure a1-17 Polar plot of sample 1-2, at different magnetic field (a) 600G, (b)800G, (c)1000G and (d)1600G

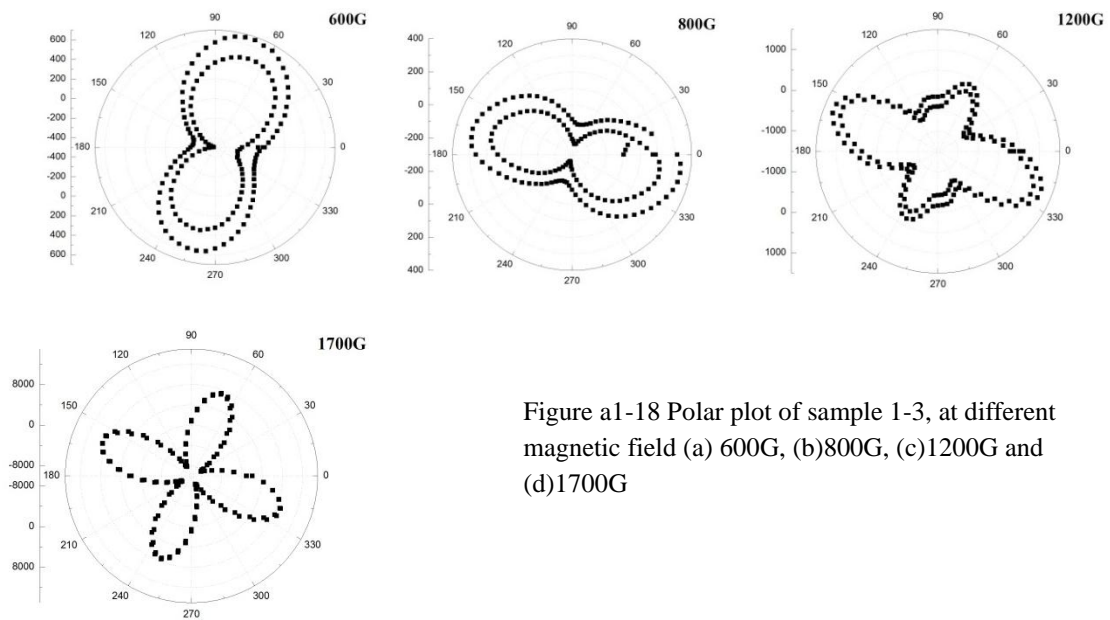


Figure a1-18 Polar plot of sample 1-3, at different magnetic field (a) 600G, (b)800G, (c)1200G and (d)1700G

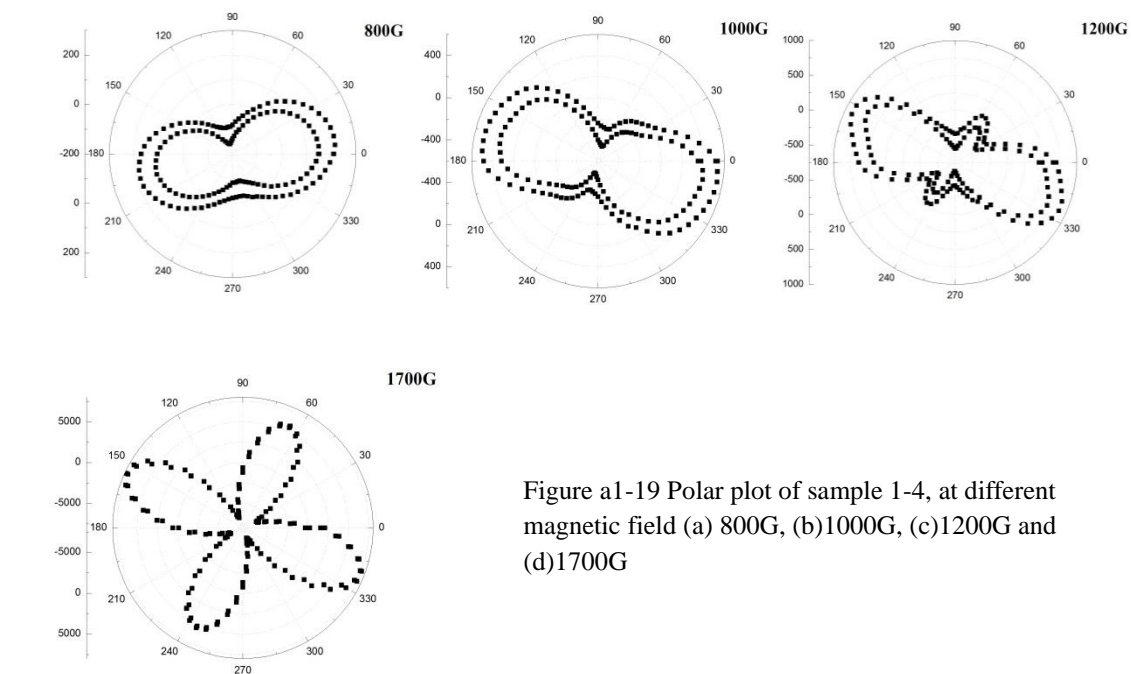


Figure a1-19 Polar plot of sample 1-4, at different magnetic field (a) 800G, (b)1000G, (c)1200G and (d)1700G

### Appendix 1.3 Magnetostriction Curves

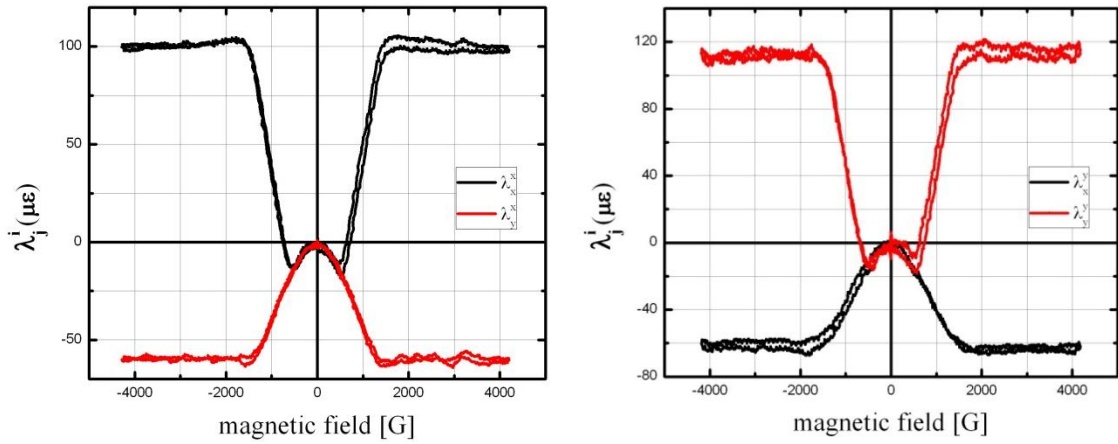


Figure a1-20 Magnetostriction of sample 1-2 under H field applied along  $\hat{x}$  (left) and  $\hat{y}$  (right)

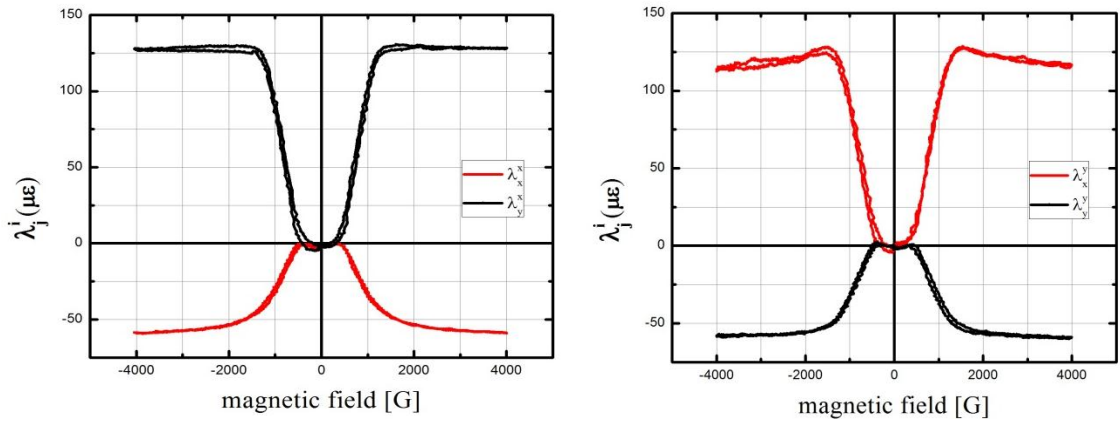


Figure a1-21 Magnetostriction of sample 1-3 under H field applied along  $\hat{x}$  (left) and  $\hat{y}$  (right)

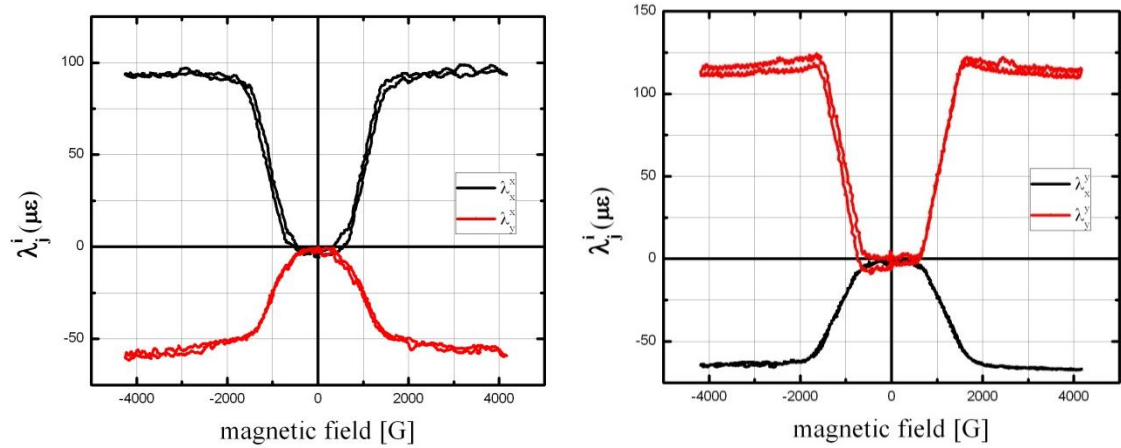


Figure a1-22 Magnetostriction of sample 1-4 under H field applied along  $\hat{x}$  (left) and  $\hat{y}$  (right)

## Appendix 2: Magnetic Domain Structures

Figure a2-1 and a2-2 are images of  $\text{Fe}_{30}\text{Co}_{70}$  polycrystalline alloy and  $\text{Fe}_{35}\text{Co}_{65}$  (sample 1-3) single crystal taken from magnetic optical Kerr microscopy (MOKE) at the remanence state. Comparing the images a2-1 and the domain images of Fe-Ga single crystals<sup>[30]</sup> (figure 1-9), large block domain pattern should be expected ( $180^\circ$  domain wall) for the Fe-Co single crystal sample disks. However, the polishing of single crystal was restricted to the sample size (a2-2).

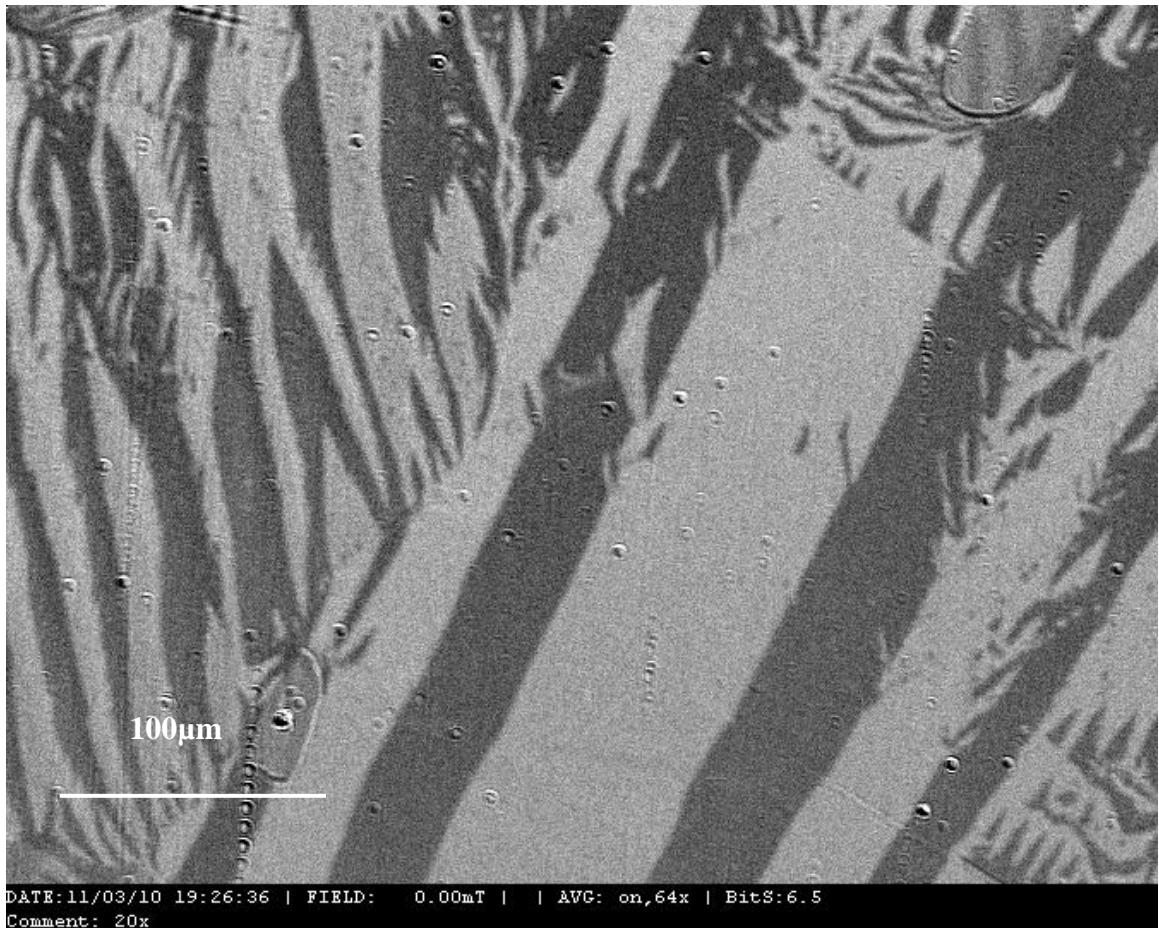


Figure a3-1  $\text{Fe}_{30}\text{Co}_{70}$  polycrystalline alloy

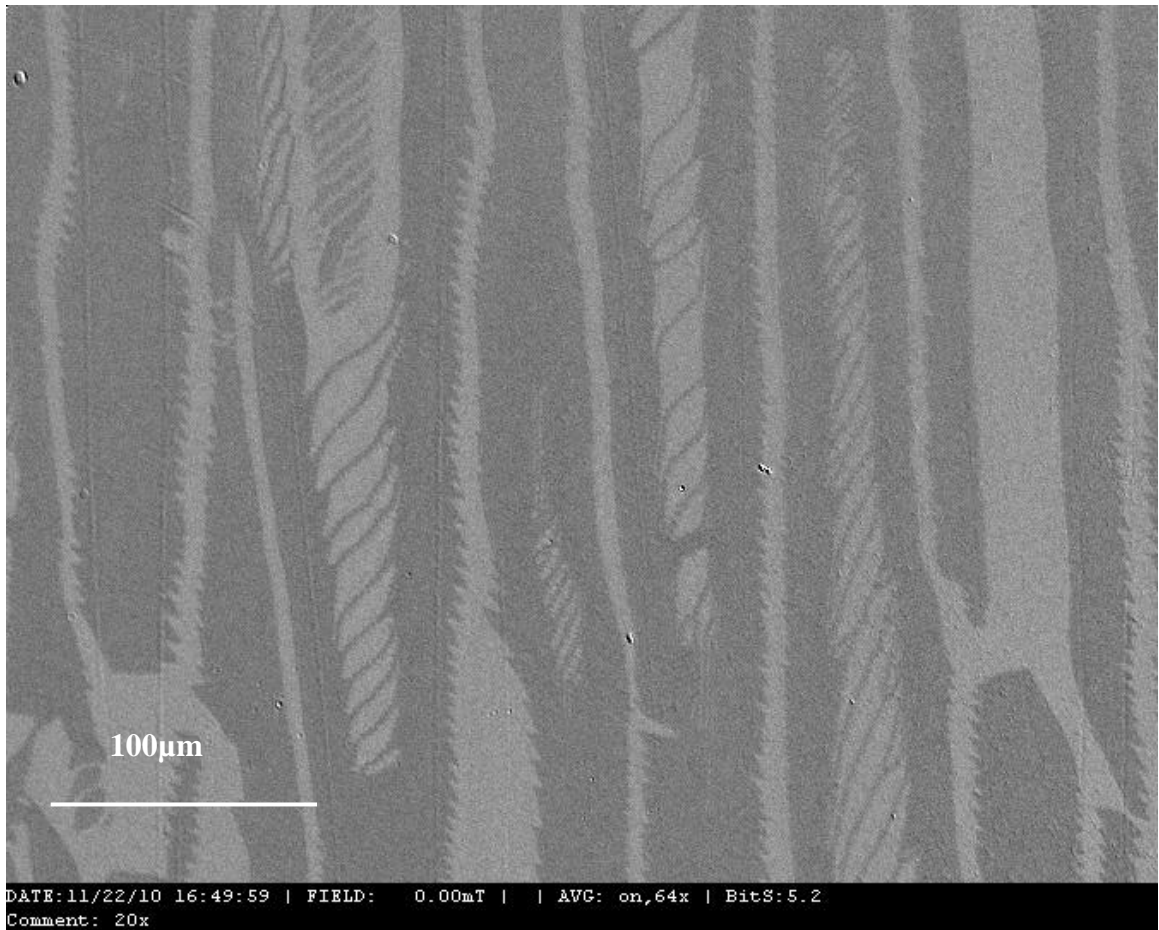


Figure a3-2  $\text{Fe}_{35}\text{Co}_{65}$  single crystal sample 1-3

## References

- [1] R. M. Bozorth, Ferromagnetism, ser. Bell Telephone Laboratories, D. Van Nostrand Company INC., New York, 1951
- [2] Elmen, G. W. U.S.P. 1 739 752, Magnetic Material and appliance, Appl. 1927
- [3] J. W. Shih, Phys. Rev. Lett., Vol. 46, Issue 2, pp. 139-142, 1934
- [4] R. S. Sundar and S. C. Deevi, ChemInform, Vol. 37, Issue 15, 2006
- [5] T. Sourmail, Scripta Materialia, Vol. 51, Issue 6, pp. 589-591, 2004
- [6] R.H. Yu et al., J. Appl. Phys., Vol. 85, Issue 8, pp. 6034-6036, 1999
- [7] Ellis, W.C. Rensselaer Polytech. Inst. Bull., Eng. Sci. Ser. 16, 1927
- [8] T. Sourmail, Progress in Materials Science, Vol. 50, Issue 7, pp. 816-880, 2005
- [9] Nishizawa and Ishida, Journal of Phase Equilibria, Vol. 5, Num. 3, pp. 250-259, 1984
- [10] J. W. Rodgers and W. R. Maddocks, "The influence of the alloying element on the  $\alpha_3$  point in iron-cobalt and other alloys", Technical report, Second alloy steels report-Section VIII, 1939.
- [11] L. Kussmann, Vol. 13, 1932
- [12] C. G. Shull and S. Siegel, Phys. Rev., Vol. 75, Issue 7, pp. 1008-1010, 1949
- [13] Ellis, W. C., Greiner, E. S., Trans. Am. Soc. Metals 29, pp. 415-432, 1941
- [14] T. Sourmail, Scripta Materialia, Vol. 52, Issue 12, pp. 1347-1351, 2005

- [15] I. Ohnuma et al., *Acta Materialia*, Vol. 50, Issue 2, pp 379-393, 2002
- [16] H. Asano et al., *Trans. Jpn. Inst. Met.*, Vol. 8, 180, 1967
- [17] G. Y. Chin and J. H. Wernick, *Ferromagnetic material*, North-Holland Pub. Co., vol. 2, (ed. E. P. Woflforth), pp. 55–188, 1980
- [18] R. C. Hall, *J. Appl. Phys.*, Vol. 30, Num. 6, pp. 816-819, 1959
- [19] R. C. Hall, *Trans. Met. Soc. AIME*, Vol. 218, pp. 268-270, 1960
- [20] R. C. O’Handley, “*Modern Magnetic Materials*”, John Wiley & Sons Inc., 2000
- [21] A. Chamberod et al., *J. Phys. Chem. Solids*, Vol. 33, pp. 593-600, 1972
- [22] S. R. Williams, *Rev. Sci. Instruments* 3, pp. 675-83, 1932
- [23] Y. Masiyama, *Sci. Repts. Tohoku Imp. Univ.* 21, pp. 394-410, 1932
- [24] L. Néel, *Magnetic Lag.*, 1951
- [25] Helen M. A. Urquhart, K. Azumi, and J. E. Goldman; Laboratory for magnetic research; August 1953; <http://handle.dtic.mil/100.2/AD018771>
- [26] L. F. Bates and E. W. Lee; private communication
- [27] L. Dai and M. Wuttig, “*Magnetostriction in Co-rich bcc FeCo Solid Solutions*”, unpublished, 2007
- [28] G. Petculescu, K. B. Hathaway, T. A. Lograsso, M. Wun-Fogle and A. E. Clark, *J. Appl., Phys.* Vol. 97, Issue 10, 10M315, 2005

- [29] S. Datta, Ph.D. dissertation, University of Maryland, College Park, MD, USA, 2009
- [30] C. Mudivarthi, Ph.D. dissertation, University of Maryland, College Park, MD, USA, 2010
- [31] R. A. Kellogg, Ph.D. dissertation, Iowa State University, 2003
- [32] A. E. Clark et al., IEEE Transactions on Magnetics, vol. 36, Issue. 5, pp. 3238–3240, 2000
- [33] R. A. Kellogg et al., Acta Materialia, vol. 52, no. 17, pp. 5043–5050, 2004
- [34] W. Heisenberg, Zeitschrift für Physik A Hadrons and Nuclei, vol. 49, pp. 619–636, 1928
- [35] A. E. Clark et al., J. Appl. Phys., Vol. 93, no. 10, pp. 8621–8623, 2003
- [36] S. Rafique, Master thesis, University of Maryland, College Park, MD, USA, 2003
- [37] A. E. Clark et al., IEEE Trans. Magn. 36, pp. 3238, 2000
- [38] J. Cullen, unpublished work
- [39] K. Honda and S. Kaya, Sci. Repts. Tohoku Imp. Univ., Vol. 15, pp. 721-754, 1934
- [40] MicroSense experimental equipment's descriptions:  
<http://www.microsense.net/Collateral/Documents/English-US/The%20Torque%20Magnetometer.pdf>
- [41] J. Kerr, Philosophical Magazine Series 5, vol. 3, no. 19, pp. 321 – 343, 1877

- [42] R. Schäfer and A. Hubert, “Magnetic Domains: the analysis of magnetic microstructures”, Springer-Verlag Berlin Heidelberg, 2009
- [43] S. Chikazumi, “Physics of Ferromagnetism”, ser. Physics of Ferromagnetism, New York: Clarendon Press, Oxford, 1997
- [44] H. J. Williams, R. M. Bozorth, and W. Shockley, *Phys. Rev.*, vol. 75, no. 1, pp. 155–178, 1949
- [45] C. Mudivarthi, *J. Magn. Magn. Mater.*, Vol. 322, Issue 14, pp. 2023-2026, 2010
- [46] A. R. Wazzan, A. Bristoti, L. B. Robinson, and A. Ahmedieh; *J. Appl. Phys.*, Vol. 44, No.5, pp. 2018-2024, 1973